

DepthCues: Evaluating Monocular Depth Perception in Large Vision Models

Duolikun Danier Mehmet Aygün Changjian Li Hakan Bilen Oisin Mac Aodha
University of Edinburgh

<https://danier97.github.io/depthcues>

Abstract

Large-scale pre-trained vision models are becoming increasingly prevalent, offering expressive and generalizable visual representations that benefit various downstream tasks. Recent studies on the emergent properties of these models have revealed their high-level geometric understanding, in particular in the context of depth perception. However, it remains unclear how depth perception arises in these models without explicit depth supervision provided during pre-training. To investigate this, we examine whether the monocular depth cues, similar to those used by the human visual system, emerge in these models. We introduce a new benchmark, *DepthCues*, designed to evaluate depth cue understanding, and present findings across 20 diverse and representative pre-trained vision models. Our analysis shows that human-like depth cues emerge in more recent larger models. We also explore enhancing depth perception in large vision models by fine-tuning on *DepthCues*, and find that even without dense depth supervision, this improves depth estimation. To support further research, our benchmark and evaluation code will be made publicly available for studying depth perception in vision models.

1. Introduction

To ensure safe, accurate, and robust interaction with the 3D world, it is important for computer vision models to understand geometric properties from their projections onto 2D images. Of particular significance is the perception of depth from single images, which has been found to benefit various downstream tasks including segmentation [43], object detection [36], and image and video generation [46, 82], among others. Monocular depth estimation models traditionally rely on dense depth supervision, but obtaining high-quality depth ground truth at scale is challenging, unlike the abundance of large 2D image-only datasets.

Large-scale pre-trained vision models like CLIP [57], Stable Diffusion [61], and DINOv2 [55], trained solely on 2D images, have shown strong generalization when fine-

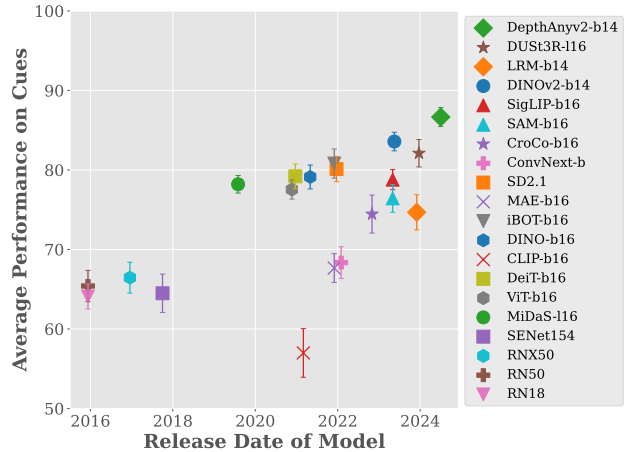


Figure 1. **Human-like monocular depth cues emerge in large vision models.** We present *DepthCues*, a comprehensive benchmark suite designed to probe the understanding of human monocular depth cues in vision models. We analyse a diverse set of vision models and find that recent self-supervised and geometry estimation models demonstrate a notably stronger grasp of these cues, even in cases where models (e.g., DINOv2) were not explicitly pre-trained on any depth-related tasks.

tuned on various computer vision tasks, including monocular depth estimation [17, 22, 81], even reaching human-level performance in ordering objects by depth [47]. As a result, numerous recent monocular depth estimation approaches [28, 39, 78] leverage these models’ depth priors to achieve state-of-the-art performance. This naturally raises an important question: *How does depth perception arise in these large vision models?*

Studies on the Human Visual System [9, 38] suggest that humans infer monocular depth using various visual cues such as elevation, light and shadow, occlusion, perspective, size, and texture gradient [7, 44] (see the top part of Fig. 2). Although these visual cues could emerge in large vision models during pre-training, it remains unclear to what extent this is true. Existing benchmarks [4, 17, 22, 47, 81] focus on evaluating the depth estimation performance of large vision models but do not investigate their understanding of the underlying visual cues. To address this gap, we eval-

uate how well the large vision models understand and utilize human-like monocular depth cues. Our goal is to provide insights into current models’ depth estimation behavior, enable a more systematic analysis of their strengths and limitations, and indicate areas for improvement.

We introduce a new benchmark named *DepthCues* consisting of six depth related tasks (see Fig. 2) where each task is designed to test a given models’ ability to estimate a visual cue that is ubiquitous to human depth perception. Specifically, lightweight probing models (referred to as the *probes* hereafter) placed on top of the frozen features of large vision models are trained and tested on the associated dataset for each task. The assumption is that the more effectively the probe can learn to solve a task using the features of a model, the better the model understands the task-specific cue. Under this protocol, we examine 20 vision models pre-trained at scale under various settings, including self-supervised learning (DINOv2 [55]), image generation (StableDiffusion) [61], vision-language supervision (CLIP [57]), single-view reconstruction (LRM [33]), cross-view completion (CroCo [72]), and also a recent general purpose depth estimation model DepthAnythingv2 [78].

Our results reveal the following observations: First, the performance of models on *DepthCues* is highly correlated with their depth estimation performance, validating the effectiveness of *DepthCues* for investigating depth perception. Second, more recent self-supervised and geometry estimation models exhibit a stronger understanding of human monocular depth cues (see Fig. 1), with DepthAnythingv2 ranking first, and DINOv2 and StableDiffusion ranking top-five. Third, none of the benchmarked models consistently excel on all six of the depth tasks. Finally, recent single-view pre-trained models are limited in their perception of texture gradient, while multi-view trained models are better at this low-level geometric cue. Additionally, we explore enhancing depth awareness of vision models by injecting depth cue priors, demonstrating that fine-tuning on our *DepthCues* benchmark results in improved depth estimation, despite the significant sparsity of the supervision compared to dense annotations. Our contributions are:

- We develop and make available *DepthCues*, a benchmark suite for evaluating the emergence of human monocular depth cues in large vision models.
- We evaluate 20 diverse vision models across a range of pre-training settings, and analyze their relative strengths and weaknesses in capturing monocular depth cues.
- We show that human depth perception cues emerge from self-supervised pre-training on single images, with stronger alignment found in more recent, larger models.
- We conduct an exploratory study on enhancing the depth awareness of a model by fine-tuning on *DepthCues*, showing that explicitly injecting human-like depth priors can improve depth perception.

2. Related Work

Monocular Depth Estimation. Monocular depth estimation is an inherently ill-posed and challenging problem, yet deep learning-based methods have made significant strides in addressing it. Initial progress was driven by supervised methods [6, 16, 19] that were trained on various labeled datasets [23, 53]. Later, self-supervised approaches advanced the field further by leveraging stereo [21, 25] or temporal consistency [26, 27, 85]. More recently, general purpose methods [39, 59, 77, 78] leveraging large vision backbone models pre-trained with self-supervised [55] or generative objectives [61] and then fine-tuned on very large-scale supervised datasets have been shown to result in strong monocular depth estimation performance. However, it remains unclear how depth perception develops in the pre-trained models without explicit depth supervision during pre-training. In this paper, we try to shed light on the emergence of these monocular depth cues used by the human visual system in large vision models.

Depth Perception in Pre-trained Vision Models. Several recent efforts have begun to analyze the 3D and depth perception abilities of pre-trained large vision models, with a focus on 3D awareness [17], 3D scene understanding [51], depth and height perception [4], and 3D physical understanding [81]. Complementary to these efforts, several studies have attempted to enhance the capabilities of these models by integrating 3D and depth information [3, 45, 79, 83]. Unlike these works, we focus on monocular depth estimation, emphasising evaluating the emergence of monocular cues essential for human depth perception. Some of the cues we study are also explored in a concurrent work [81], however, we focus on depth perception with diverse data and analyze a broader range of vision models.

Recent work [22, 65] has analyzed monocular depth estimation models, examining properties like the backbone architectures, loss functions, and training datasets. However, they do not explore whether or how these models actually utilize monocular cues for depth estimation. In our work, we focus on analyzing the existence of intrinsic depth cues without direct depth supervision across various large vision models. Closely related to our approach, [66] investigates whether predictions of a monocular depth estimation model [59] violate perceptual cues. However, a prediction that violates a perceptual cue does not necessarily indicate the absence of the cue in the model itself. Instead, we directly examine the presence of these cues across multiple models, including, but not limited to, monocular depth models using our newly introduced benchmark suite.

Comparing Humans to Neural Networks. Human and animal vision systems have long inspired computational vision methods [31, 37, 56]. Many studies have sought to compare biological vision with modern neural network-based computer vision systems across tasks such as ob-

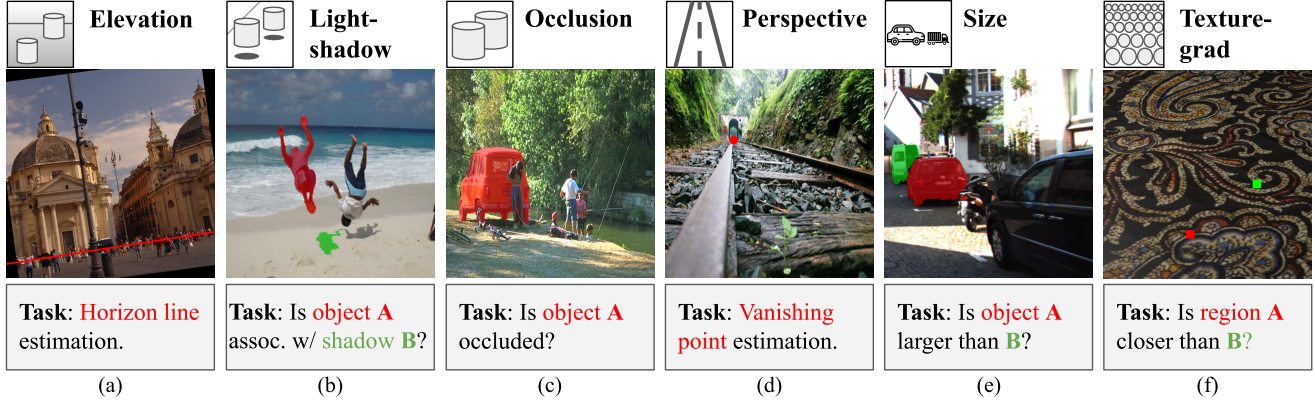


Figure 2. **Overview of *DepthCues*.** Monocular depth cues, the associated tasks, and example instances from our proposed benchmark.

Depth Cue	Source	#Images	#Train	#Val	#Test
Elevation	HLW [75]	18,390	15,761	828	1,801
Light-shadow	SOBA [71]	798	4,716	862	860
Occlusion	COCOA [88]	5,573	24,402	12,906	14,862
Perspective	NaturalScene [86]	2,275	2,000	125	150
Size	KITTI [23], SUN [64]	2,717	1,986	330	712
Texture-grad	DTD [12]	6,000	4,000	1,000	1,000

Table 1. **Summary of the datasets in *DepthCues* benchmark.** We report total image and data statistics across all splits.

ject recognition [58], shape-bias [24], multi-view consistency [8, 54], visual perspective-taking [47], and perceptual judgments of similarity [20]. In our work, rather than measuring alignment between human and large-scale vision systems, we focus on the emergence of monocular cues that are well-established in the human vision science community [7, 9, 38, 44], *i.e.*, the cues that are crucial for monocular depth estimation in human vision. Recent work has incorporated additional *high*-level human vision-inspired cues, specifically semantics, object size, and spatial relationships, in an attempt to improve automated monocular depth estimation [1, 2]. These cues, extracted using pre-trained semantic segmentation and language embedding models, are shown to enhance depth prediction accuracy. We hope that our results and analyses will inspire similar approaches and foster new directions.

3. *DepthCues*: Benchmark and Dataset

We introduce *DepthCues*, a new benchmark to investigate how large-scale pre-trained image models perceive depth by assessing their understanding of a set of monocular depth cues used by humans to perceive depth: elevation, light and shadow, occlusion, perspective, size, and texture gradient [9, 38]. Our benchmark comprises a suite of six tasks with constituent datasets specifically designed to capture the essence of each individual monocular depth cue. For each task, *DepthCues* provides training and test sets with an evaluation protocol for image models, along with a performance metric to assess how well a given model under-

stands each depth cue. Fig. 2 illustrates the task for each cue, and shows a representative instance from the associated dataset. We summarize the statistics of our datasets in Tab. 1. Next, we describe the construction of each task and the data used. In each case, we adapt existing datasets that have been designed for bespoke vision tasks. We use the original train, validation, and test splits of data sources and keep the classes balanced for binary tasks unless specified. Additional details about dataset construction are provided in Appendix B.

3.1. Elevation

Objects on the ground plane are farther away as they get closer to the horizon.

Task. The elevation cue relies on perceiving the horizon line, which is defined as the projection of all the points where light rays from the observer’s viewpoint are tangent to Earth’s surface. Therefore, we adopt the task of horizon line estimation [42, 75]. Note, the horizon line is not always visible, and is different from the skyline, which separates the sky and the entities on the ground. The task is posed as a regression problem where the goal is to estimate the target line, *i.e.*, its slope and y-intercept, in the image.

Dataset. We adopt the HLW dataset [75], which provides pairs of images and annotations of the horizon lines. To increase the slope variation, we augment the images by rotating them (and the line annotations) randomly between -30° and 30° . An example from the dataset is shown in Fig. 2 (a).

3.2. Light and Shadow

The way shadow is cast provides useful cue for orientation and depth of objects. For convenience, we refer to this cue as light-shadow.

Task. To capture the understanding of this cue, we propose a task of associating shadows with objects.

Dataset. The SOBA [71] dataset contains images with segmentation masks of objects and their associated shadows. From those, we create a dataset containing tuples of

(I, M_A, M_B, y) , where M_A is the mask of the object A in image I , and M_B is the mask of a shadow B in the image. The label y is 1 if B is associated with A , and 0 otherwise. An example is depicted in Fig. 2 (b).

3.3. Occlusion

An object that partially blocks another, from the perspective of the viewer, is perceived as closer.

Task. To test whether models understand occlusion, we propose the task of identifying whether an object is occluded or not by another object.

Dataset. We use the COCOA [88] dataset, providing manually annotated segmentation masks for visible and invisible object parts with occlusion rates. From the original annotations, we construct a dataset that contains triplets of image I , the segmentation mask M_A of the visible part of the object A , and the corresponding label y , which is 1 if the object is occluded, and 0 otherwise. In the example in Fig. 2 (c), the car highlighted with a red mask is occluded.

3.4. Perspective

Parallel lines converging at infinity offer a strong cue for perceiving depth.

Task. This cue is closely tied to vanishing point [48], which is defined as the point on the image plane where 2D perspective projections of 3D parallel lines intersect. Therefore, we use the task of vanishing point estimation to investigate the understanding of perspective. While there exist different versions of the task that define different numbers of vanishing points [67], we adopt a simplified version that focuses on a single dominant vanishing point. Given an image I , the objective is to estimate the $\mathbf{p} = (x, y)$ coordinates of the vanishing point in the image coordinate system.

Dataset. The NaturalScene dataset [86] contains images from diverse outdoor scenes with one manually annotated dominant vanishing point \mathbf{p} in each. We use the original dataset and create validation and test sets by dividing the original validation set. An example is shown in Fig. 2 (d) with the vanishing point indicated by the red dot.

3.5. Size

People infer depth based on known object sizes (in 3D) and their apparent retinal sizes (*e.g.*, an object farther away appears smaller). This cue is particularly effective when comparing objects of similar expected sizes.

Task. Using this cue requires prior knowledge of object sizes. Thus we propose a binary classification task: determining if object A is larger than object B in 3D.

Dataset. We use 3D object detection datasets KITTI [23] and SUN-RGBD [64] which provide 3D bounding boxes of objects in outdoor and indoor scenes respectively. Given an image I , we sample two objects, A and B , and compare their sizes using the volumes of their 3D bounding boxes.

Object masks M_A and M_B in image space are estimated using SAM [41] with bounding box queries and additional filtering to ensure segmentation quality. The final dataset contains tuples (I, M_A, M_B, y) , where the label $y = 1$ if object A is larger, and 0 otherwise. We filtered pairs where the volume difference was under a threshold to reduce errors caused by imprecise labeling. See Fig. 2 (e) for an example.

3.6. Texture Gradient

When a region on a surface is further away from the viewer, its texture appears denser and more compressed, with a higher spatial frequency, compared to the same texture viewed nearby. We denote this cue as texture-grad.

Task. This cue is especially helpful on textured surfaces. To assess the existence of this cue, we use the task of depth ordering of regions on a textured plane, where the model must infer depth based solely on texture.

Dataset. To ensure that only the texture gradient cue is used for perceiving depth order, we created a synthetic dataset using Blender. First, we initialized a 3D plane, and applied textures sampled from the DTD dataset [12] which contains various real-world, as well as synthetic, textures. Then, fixing both the viewing direction of the camera (to always point at the plane center) and its distance to the plane center, we randomly set the camera elevation angle between 30° and 60° , and project the textured plane on the camera imaging plane to obtain an image with its depth map.

From each image I , we randomly sample two equal-sized regions A and B (with their masks M_A, M_B), then set label y to 1 if A is closer than B and 0 otherwise. To avoid the region higher up in the image always being farther away, we apply random horizontal and vertical flips, so that the task cannot be solved solely from locations of the regions. An example image is shown in Fig. 2 (f).

4. Evaluation Protocol

Following previous work [17, 81], we use probing of visual features as our evaluation protocol. Below, we explain how we obtain task-specific input features from visual models, how we probe these features, and how we measure success. An illustrative figure is included in Appendix C.1.

4.1. Task Specific Visual Features

Given a pre-trained vision model $\phi(\cdot)$, we assess its understanding of a cue by training a lightweight probe g_θ with parameters θ on the target task, using the features extracted by ϕ . We obtain features \mathbf{f} for each task as described below. **Occlusion.** We extract a feature map $\phi(I)$ from the image I and up-sample it to match the spatial size of the object mask M_A . We mask the feature map and apply spatial pooling:

$$\mathbf{f} = \frac{\sum_{h,w} M_A \odot \text{up}(\phi(I))}{\sum_{h,w} M_A}, \quad (1)$$

where h, w index the height and width of I , \odot is element-wise multiplication, and $\text{up}(\cdot)$ denotes bilinear up-sampling. This results in $\mathbf{f} \in \mathbb{R}^D$ where D is the feature dimension and changes depending on the vision model ϕ .

Light-shadow, Size, and Texture-grad. For these tasks, we calculate the difference between the masked average features of objects A and B :

$$\mathbf{f} = \frac{\sum_{h,w} M_A \odot \text{up}(\phi(I))}{\sum_{h,w} M_A} - \frac{\sum_{h,w} M_B \odot \text{up}(\phi(I))}{\sum_{h,w} M_B}. \quad (2)$$

Elevation and Perspective. These tasks are not object/region specific, so we use the entire image feature, *i.e.*, $\mathbf{f} = \phi(I) \in \mathbb{R}^{H_f \times W_f \times D}$, where H_f, W_f are the height and width of the feature map.

4.2. Probing Features

For light-shadow, occlusion, size, and texture-grad, where the task-specific features \mathbf{f} are D -dimensional vectors, we implement the probe g_θ as a multi-layer perception (MLP) with two layers and an intermediate GELU activation [32]. Though linear probing has been used commonly for probing large vision models [55], it is not obvious that the solutions to our tasks should be a linear function of the model features. Thus, we use non-linear probes, which empirically outperform linear probes (see Appendix A.2). For elevation and perspective, which require global information, we use an attentive probe [5, 18]. This probe aggregates global features through cross-attention and uses a two-layer MLP for final predictions. We observed via empirical results that the attentive probe achieves better performance than a standard MLP probe on these tasks.

Training and Optimization. We train the MLP probes for light-shadow, occlusion, size and texture-grad tasks using binary cross-entropy loss, as these tasks involve binary classification. For elevation and perspective, we use mean squared error loss to train the attentive probes, as the tasks are formulated as regression problems. Additional details on the probe optimization are provided in Appendix C.1.

Following [55, 81], we perform a hyper-parameter search on the layers of model ϕ . For each task, we extract features from different layers of ϕ , and train a probe on these features under the same setting. The best layer is then selected based on the validation performance, and the probing on this layer is repeated five times using different random seeds. We report the mean and standard deviation of the test performance.

4.3. Evaluation Metrics

For light-shadow, occlusion, size and texture-grad which are binary tasks, we report classification accuracy. For the vanishing point estimation task of the perspective cue, while Euclidean distance (between the predicted and ground-truth

vanishing points) is a sensible metric, we instead report success rate to align this metric more closely with accuracy. Specifically, if the Euclidean distance of a prediction falls below a pre-defined threshold, it is interpreted as success. For elevation, we convert the horizon detection error [75] to an accuracy-based measure using a similar approach. More details are provided in Appendix C.2.

5. Experiments

5.1. Monocular Depth Cues in Vision Models

We evaluate 20 pre-trained large vision models [10, 15, 29, 30, 33, 35, 41, 49, 55, 57, 59, 61, 68, 70, 72, 76, 78, 80, 84] spanning diverse pre-training objectives, modalities, and model architectures to assess their understanding of monocular depth perception cues in our *DepthCues* benchmark.

Implementation Details. Where possible, we focus on model architectures equivalent to ViT-Base and denote the architecture size (and patch size for transformers) using postfixes, *e.g.*, DINOv2-b14. More details about the models and their architecture are provided in Appendix D. For consistency, we use only patch tokens for all ViT-based models [15], as some do not include a class token.

Additional Baselines. During the probing of certain cues, we explicitly use mask information to construct the input feature, f . Although these masks are not directly used by the probes, they could theoretically be leveraged to solve tasks. To verify that any additional information from this step is insufficient to solve the task, we designed a *trivial baseline* in which model features are replaced with simple 2D coordinate maps *i.e.*, $\phi(I)$ in Eqs. (1) and (2) becomes $C \in \mathbb{R}^{H \times W \times 2}$ where $C_{h,w} = [h, w]^T$. Moreover, for each cue, we include an *end-to-end* baseline, where we train ResNet18 [29] and ViT-B/16 [15] models from scratch in an end-to-end fashion and select the best. We concatenate the masks with the input images channel-wise, allowing us to assess how much of each task can be solved without relying on sophisticated pre-trained features. Finally, to confirm that the tasks are readily solvable by humans, we evaluate our own performance on a random sample from the test sets, and obtained an accuracy of $95\% \pm 1.48\%$ across tasks.

Additional Tasks. To extend our analysis, we also evaluate vision models for monocular depth estimation (on NYUv2 [63]) and image classification (on ImageNet-1k [14]) using a linear probe, a standard approach in previous work [3, 55, 79] for probing these datasets. Following the previous works [6, 11, 17], For NYUv2, we report accuracy as the percentage of pixels where the ratio between predicted and ground-truth depth is less than 1.25. We report top-1 accuracy for ImageNet. More details on these tasks are provided in Appendix A.1, and we show the linear probing results of these models on NYUv2 in Fig. 3.

Results. The probing results of 20 pre-trained vision mod-

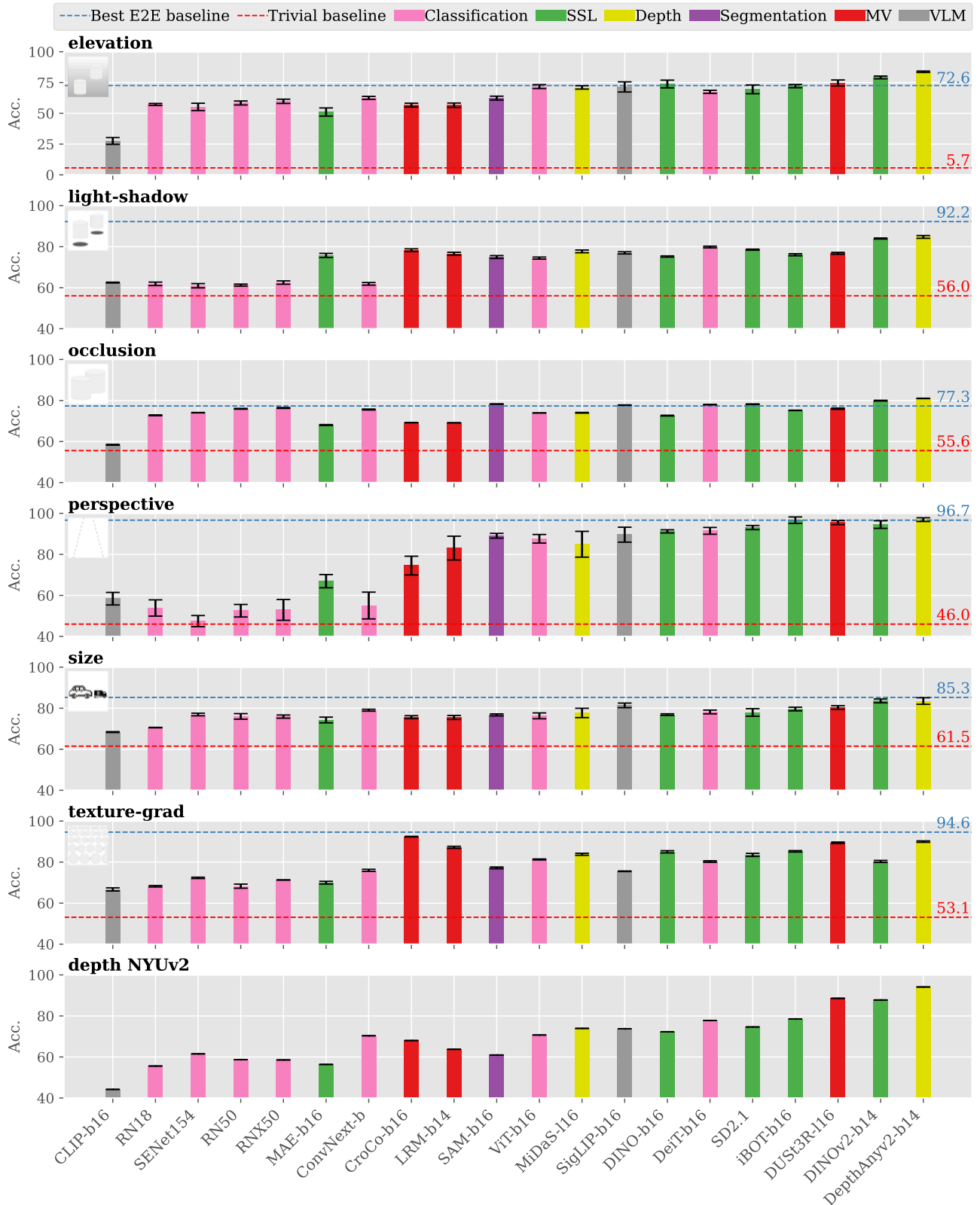


Figure 3. **DepthCues Benchmark Results.** We evaluate 20 vision models with diverse pre-training settings (indicated by color) on the *DepthCues* benchmark, which assesses six different monocular depth cues (each row) ubiquitous to humans. The models are ranked based on their average performance on the six cues. We include an end-to-end trained baseline (blue dotted line) as an oracle and a trivial baseline (red dotted line) to mark floor performance. Additionally, depth estimation linear probing results on NYUv2 are shown on the bottom row.

els and the additional baselines on our *DepthCues* benchmark are summarized in Fig. 3, where the models are ranked by average performance over all cues. Moreover, we measured Spearman Ranked-order Correlation between each pair of tasks in *DepthCues* using the ranks of the models evaluated, and also how they correlate with the depth estimation and image classification performance of models, which is visualized in Fig. 4. We discuss our observations below, and present additional analysis, such as how pre-training data size impacts performance, in Appendix A.1.

(i) Depth cues emerge in more recent large vision models. Firstly, the specialized depth estimation model, DepthAnythingv2, achieved the highest overall performance on *DepthCues*, indicating the possibility that it leverages such cues to estimate depth. We also observe the emergence of human-like monocular depth cues in recent large vision models, such as DINOv2 and Stable Diffusion. Notably, newer large vision models demonstrate a stronger grasp of these depth cues, as illustrated in Fig. 1. DINOv2 and Stable Diffusion have proven useful for developing monocular depth estimation models [39, 78]. However, the reasons behind these models’ effectiveness for depth inference remain unclear, given the lack of explicit depth supervision during pre-training. Our results provide an insight on the development of depth perception in these models: they develop an awareness of human-like monocular depth cues, which might aid depth inference.

(ii) Depth models do not always have the strongest knowledge of depth cues. While DepthAnythingv2 achieves the best overall performance on *DepthCues*, another specialized depth estimation model, MiDaS, is outperformed by several models pre-trained without depth supervision, *e.g.*, DeiT, SigLIP, and DINO. These models also exhibit competitive depth estimation performance (under linear probing) to MiDaS. This suggests that other pre-training recipes than dense depth supervision can effectively enhance depth perception, although they may be less data-efficient – for instance, SigLIP is trained on around 10,000 times more data than MiDaS.

(iii) Vision-language models exhibit varying levels of depth cue understanding. CLIP obtains the lowest performance on *DepthCues*, explaining its limited depth estimation ability as seen in Fig. 3 and in recent work [17]. CLIP’s limited understanding of the visual concepts tested in *DepthCues* may present challenges for downstream tasks that require geometric understanding [87]. In contrast, SigLIP, also trained on matching images to captions but on significantly more data ($\times 9$ more data than CLIP), has a significantly better grasp of the depth cues.

(iv) Multi-view models are better at the texture-grad task than single-view models. On all depth cues except texture-grad, recent models which are pre-trained with single-view images showed overall better performance than

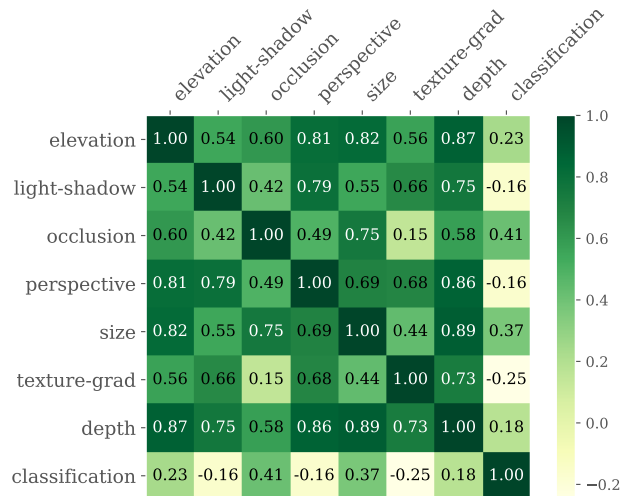


Figure 4. **Task correlation.** We measure the Spearman Ranked-order Correlation between each pair of tasks in *DepthCues* benchmark, and how they correlate with depth estimation and image classification performance of models. A correlation score of one indicates the same ranking of models for two tasks.

multi-view ones. However, on texture-grad, all three multi-view models (*i.e.*, CroCo, LRM, and DUST3R) ranked within the top four, outperforming strong SSL competitors such as DINOv2. While the other five cues operate at the scene or object level, texture-grad uniquely requires a more localized, surface-level understanding. Multi-view pre-trained models are often more effective at capturing such details than single-view models because, during pre-training, they are exposed to variations in the same surface across different viewpoints. For instance, CroCo, which achieves the best performance on the texture-grad task, is trained to reconstruct parts of a scene from different viewpoints, requiring attention to finer local details. Moreover, LRM and DUST3R are pre-trained on 3D object and scene reconstruction tasks, which require understanding correspondences across views by leveraging local surface details.

(v) Performance on *DepthCues* correlates with depth estimation performance. As shown in Fig. 4, all *DepthCues* tasks exhibit moderate to high levels of correlation with depth estimation, supporting the importance of depth cues for this task. However, all tasks have a low correlation with ImageNet-1k classification. Interestingly, a relatively higher alignment with classification is observed for occlusion and size, which are also highly correlated with each other. This is reasonable as understanding occlusion and size requires object-level semantics (*e.g.*, ‘What does the recognized object look like when not occluded?’ and ‘Is category A larger than category B?’). Apart from texture-grad, each cue has a high correlation (> 0.75) with at least one other cue. As discussed above, the texture-grad cue requires understanding surface details and provides local-

Model	NYUv2 Acc. (%) \uparrow	DIW WHDR (%) \downarrow
DINOv2	87.78	11.99
DINOv2+DC	87.06	11.95
concat(DINOv2, noise)	87.56	12.20
concat(DINOv2, DINOv2+DC)	88.46	11.72
CLIP	43.78	35.25
CLIP+DC	43.59	35.45
concat(CLIP, noise)	43.38	35.39
concat(CLIP, CLIP+DC)	44.32	33.53

Table 2. **Linear probing on downstream depth estimation.** For each model, we probe the patch tokens from the final layer. Models with '+DC' are fine-tuned using supervision on our *DepthCues* benchmark. The best results in each subset are **bolded**.

ized depth information; perception of this cue is found to be weaker in single-view image models. We note that texture-grad is the only cue that uses synthetic data, which might also contribute to its lower correlation with other cues.

5.2. Learning Depth Cues

We observed that the depth estimation performance of a model highly correlates with its awareness of human-like monocular depth cues. Here we ask if enhanced depth cue awareness improves depth estimation? To investigate this, we fine-tune single-image pre-trained vision models on the training set of *DepthCues* in a multi-task manner, then evaluate the fine-tuned model on downstream depth estimation. Here we focus on two models widely adopted for various downstream applications: DINOv2 and CLIP.

We use low-rank adaptation (LoRA) [34] for efficient fine-tuning of pre-trained models. Further details of multi-task learning and LoRA implementation are provided in Appendix C.3. We evaluate the pre-trained and fine-tuned models on NYUv2 [63] and DIW [11] depth datasets using linear probes. We experiment with two different variations: first, we evaluate the features from fine-tuned models (denoted as +DC in Tab. 2); second, we concatenate the features from fine-tuned models with the features from the original pre-trained models. The latter approach was also adopted in [52, 79] to preserve the generalization ability of the pre-trained models. As before, we report accuracy for NYUv2, and use Weighted Human Disagreement Rate (WHDR) to measure performance on DIW. It is noted the dataset for the size cue in *DepthCues* contains a subset of NYUv2 images (due to the use of SUNRGBD), so evaluation on DIW offers a fairer comparison.

We observe in Tab. 2 that for both models, fine-tuning on *DepthCues* resulted in improved depth perception. Notably, the fine-tuned features often need to be concatenated with the original features to bring improvements, a similar observation also made in previous works [52, 79]. A possible explanation for the decreased generalization in the models is due to the limited size and diversity of the fine-tuning data in *DepthCues*. We also investigate whether the improvements in the concatenated variations come from the

increased parameters in the probe (due to higher dimensional input), by training linear probes on a combination of original model features and random noise (denoted as `concat(., noise)`), which did not result in improvements.

5.3. Discussion

The results in Sec. 5.1 indicate that recent large vision models understand several human-like monocular depth cues, with performance on these cues correlating with depth estimation performance. This suggests that models may use such cues to infer depth, even without explicit depth supervision. For example, the popular self-supervised model, DINOv2, has developed features that help reason about these cues (except texture-grad), which can support depth estimation. Interestingly, the results in Sec. 5.2 show that *DepthCues* enables the learning of depth cues, which benefit downstream depth performance in a linear probing setting, even though *DepthCues* has a moderate size (fewer than 35k training images, much smaller than the large datasets used to pre-train the base models), is not designed specifically for end-to-end fine-tuning, and only provides image-level sparse annotations (as opposed to dense depth maps). This suggests promising directions for enhancing depth estimation from sparse annotations.

Limitations. Our analysis focuses only on widely used pre-trained model weights but not directly on the impact of various pre-training objectives and their training datasets on the emergence of depth cues. While depth from ego-motion and scene motion are also important cues for humans, our focus is primarily on assessing monocular cues learned by large vision models trained on static image collections and not image sequences, except CroCo, LRM, and DUST3R.

6. Conclusions

We introduced *DepthCues*, a benchmark suite for evaluating human-like monocular depth cues in large vision models. Testing 20 diverse models, we found that depth perception cues, similar to those used by humans, emerge across various pre-training objectives, with more recent and larger models demonstrating stronger alignment with human depth perception. Furthermore, our fine-tuning experiments on *DepthCues* indicate that a model’s depth perception can be enhanced by explicitly incorporating human-like depth priors, suggesting promising directions for improving depth performance in future models. We hope *DepthCues* will serve as a valuable resource for advancing research in depth-aware vision systems, particularly for applications requiring robust 3D spatial understanding from 2D inputs.

Acknowledgments. Funding was provided by ELIAI (the Edinburgh Laboratory for Integrated Artificial Intelligence), EPSRC (grant no. EP/W002876/1).

References

- [1] Dylan Auty and Krystian Mikolajczyk. Monocular depth estimation using cues inspired by biological vision systems. In *ICPR*, 2022. 3
- [2] Dylan Auty and Krystian Mikolajczyk. Language-based depth hints for monocular depth estimation. *arXiv:2403.15551*, 2024. 3
- [3] Mehmet Aygun, Prithviraj Dhar, Zhicheng Yan, Oisin Mac Aodha, and Rakesh Ranjan. Enhancing 2d representation learning with a 3d prior. In *CVPR Workshops*, 2024. 2, 5
- [4] Shehreen Azad, Yash Jain, Rishit Garg, Yogesh S Rawat, and Vibhav Vineet. Geometer: Probing depth and height perception of large visual-language models. *arXiv:2408.11748*, 2024. 1, 2
- [5] Adrien Bardes, Quentin Garrido, Jean Ponce, Xinlei Chen, Michael Rabbat, Yann LeCun, Mido Assran, and Nicolas Ballas. Revisiting feature prediction for learning visual representations from video. *TMLR*, 2024. Featured Certification. 5, 14
- [6] Shariq Farooq Bhat, Ibraheem Alhashim, and Peter Wonka. Adabins: Depth estimation using adaptive bins. In *CVPR*, 2021. 2, 5, 19
- [7] Rositsa Bogdanova, Pierre Boulanger, and Bin Zheng. Depth perception of surgeons in minimally invasive surgery. *Surgical innovation*, 2016. 1, 3
- [8] Tyler Bonnen, Stephanie Fu, Yutong Bai, Thomas O’Connell, Yoni Friedman, Nancy Kanwisher, Joshua B. Tenenbaum, and Alexei A. Efros. Evaluating multiview object consistency in humans and image models. In *NeurIPS*, 2024. 3
- [9] David Bull and Fan Zhang. *Intelligent image and video compression: communicating pictures*. Academic Press, 2021. 1, 3
- [10] Mathilde Caron, Hugo Touvron, Ishan Misra, Hervé Jégou, Julien Mairal, Piotr Bojanowski, and Armand Joulin. Emerging properties in self-supervised vision transformers. In *ICCV*, 2021. 5, 19, 20, 21
- [11] Weifeng Chen, Zhao Fu, Dawei Yang, and Jia Deng. Single-image depth perception in the wild. *NeurIPS*, 2016. 5, 8, 20
- [12] M. Cimpoi, S. Maji, I. Kokkinos, S. Mohamed, , and A. Vedaldi. Describing textures in the wild. In *CVPR*, 2014. 3, 4
- [13] Matt Deitke, Ruoshi Liu, Matthew Wallingford, Huong Ngo, Oscar Michel, Aditya Kusupati, Alan Fan, Christian Laforte, Vikram Voleti, Samir Yitzhafk Gadre, et al. Objaverse-xl: A universe of 10m+ 3d objects. *NeurIPS*, 2024. 20
- [14] Jia Deng, Wei Dong, Richard Socher, Li-Jia Li, Kai Li, and Li Fei-Fei. Imagenet: A large-scale hierarchical image database. In *CVPR*, 2009. 5, 12, 20
- [15] Alexey Dosovitskiy, Lucas Beyer, Alexander Kolesnikov, Dirk Weissenborn, Xiaohua Zhai, Thomas Unterthiner, Mostafa Dehghani, Matthias Minderer, Georg Heigold, Sylvain Gelly, Jakob Uszkoreit, and Neil Houlsby. An image is worth 16x16 words: Transformers for image recognition at scale. *ICLR*, 2021. 5, 20, 21
- [16] David Eigen, Christian Puhrsch, and Rob Fergus. Depth map prediction from a single image using a multi-scale deep network. *NeurIPS*, 2014. 2
- [17] Mohamed El Banani, Amit Raj, Kevis-Kokitsi Maninis, Abhishek Kar, Yuanzhen Li, Michael Rubinstein, Deqing Sun, Leonidas Guibas, Justin Johnson, and Varun Jampani. Probing the 3d awareness of visual foundation models. In *CVPR*, 2024. 1, 2, 4, 5, 7, 12, 14, 15, 19
- [18] Alaaeldin El-Nouby, Michal Klein, Shuangfei Zhai, Miguel Angel Bautista, Alexander Toshev, Vaishaal Shankar, Joshua M Susskind, and Armand Joulin. Scalable pre-training of large autoregressive image models. In *ICML*, 2024. 5, 14
- [19] Huan Fu, Mingming Gong, Chaohui Wang, Kayhan Batmanghelich, and Dacheng Tao. Deep ordinal regression network for monocular depth estimation. In *CVPR*, 2018. 2
- [20] Stephanie Fu, Netanel Tamir, Shobhita Sundaram, Lucy Chai, Richard Zhang, Tali Dekel, and Phillip Isola. Dreamsim: Learning new dimensions of human visual similarity using synthetic data. *NeurIPS*, 2024. 3
- [21] Ravi Garg, Vijay Kumar Bg, Gustavo Carneiro, and Ian Reid. Unsupervised cnn for single view depth estimation: Geometry to the rescue. In *ECCV*, 2016. 2
- [22] Yongtao Ge, Guangkai Xu, Zhiyue Zhao, Libo Sun, Zheng Huang, Yanlong Sun, Hao Chen, and Chunhua Shen. Geobench: Benchmarking and analyzing monocular geometry estimation models. *arXiv:2406.12671*, 2024. 1, 2, 14
- [23] Andreas Geiger, Philip Lenz, and Raquel Urtasun. Are we ready for autonomous driving? the kitti vision benchmark suite. In *CVPR*, 2012. 2, 3, 4, 17
- [24] Robert Geirhos, Patricia Rubisch, Claudio Michaelis, Matthias Bethge, Felix A. Wichmann, and Wieland Brendel. Imagenet-trained CNNs are biased towards texture; increasing shape bias improves accuracy and robustness. In *ICLR*, 2019. 3
- [25] Clément Godard, Oisin Mac Aodha, and Gabriel J Brostow. Unsupervised monocular depth estimation with left-right consistency. In *CVPR*, 2017. 2
- [26] Clément Godard, Oisin Mac Aodha, Michael Firman, and Gabriel J Brostow. Digging into self-supervised monocular depth estimation. In *CVPR*, 2019. 2
- [27] Ariel Gordon, Hanhan Li, Rico Jonschkowski, and Anelia Angelova. Depth from videos in the wild: Unsupervised monocular depth learning from unknown cameras. In *ICCV*, 2019. 2
- [28] Ming Gui, Johannes S Fischer, Ulrich Prestel, Pingchuan Ma, Dmytro Kotovenko, Olga Grebenkova, Stefan Andreas Baumann, Vincent Tao Hu, and Björn Ommer. Depthfm: Fast monocular depth estimation with flow matching. *arXiv:2403.13788*, 2024. 1
- [29] Kaiming He, Xiangyu Zhang, Shaoqing Ren, and Jian Sun. Deep residual learning for image recognition. In *CVPR*, 2016. 5, 20, 21
- [30] Kaiming He, Xinlei Chen, Saining Xie, Yanghao Li, Piotr Dollár, and Ross Girshick. Masked autoencoders are scalable vision learners. In *CVPR*, 2022. 5, 20, 21
- [31] Donald Olding Hebb. *The organization of behavior: A neuropsychological theory*. Psychology press, 2005. 2

- [32] Dan Hendrycks and Kevin Gimpel. Gaussian error linear units (gelus). *arXiv:1606.08415*, 2016. 5, 20
- [33] Yicong Hong, Kai Zhang, Jiuxiang Gu, Sai Bi, Yang Zhou, Difan Liu, Feng Liu, Kalyan Sunkavalli, Trung Bui, and Hao Tan. Lrm: Large reconstruction model for single image to 3d. *ICLR*, 2024. 2, 5, 20, 21
- [34] Edward J Hu, yelong shen, Phillip Wallis, Zeyuan Allen-Zhu, Yuanzhi Li, Shean Wang, Lu Wang, and Weizhu Chen. LoRA: Low-rank adaptation of large language models. In *ICLR*, 2022. 8, 20
- [35] Jie Hu, Li Shen, and Gang Sun. Squeeze-and-excitation networks. In *CVPR*, 2018. 5, 20, 21
- [36] Kuan-Chih Huang, Tsung-Han Wu, Hung-Ting Su, and Winston H Hsu. Monodr: Monocular 3d object detection with depth-aware transformer. In *CVPR*, 2022. 1
- [37] David H Hubel and Torsten N Wiesel. Receptive fields and functional architecture of monkey striate cortex. *The Journal of Physiology*, 1968. 2
- [38] Michael Kalloniatis and Charles Luu. The perception of depth. *Webvision-the organization of the retina and visual system*, 2011. 1, 3
- [39] Bingxin Ke, Anton Obukhov, Shengyu Huang, Nando Metzger, Rodrigo Caye Daudt, and Konrad Schindler. Repurposing diffusion-based image generators for monocular depth estimation. In *CVPR*, 2024. 1, 2, 7
- [40] Diederik P. Kingma and Jimmy Ba. Adam: A method for stochastic optimization. In *ICLR*, 2015. 19, 20
- [41] Alexander Kirillov, Eric Mintun, Nikhila Ravi, Hanzi Mao, Chloe Rolland, Laura Gustafson, Tete Xiao, Spencer Whitehead, Alexander C Berg, Wan-Yen Lo, et al. Segment anything. In *ICCV*, 2023. 4, 5, 18, 20, 21
- [42] Florian Kluger, Hanno Ackermann, Michael Ying Yang, and Bodo Rosenhahn. Temporally consistent horizon lines. In *ICRA*, 2020. 3
- [43] Dong Lao, Fengyu Yang, Daniel Wang, Hyoungeob Park, Samuel Lu, Alex Wong, and Stefano Soatto. On the viability of monocular depth pre-training for semantic segmentation. In *ECCV*, 2024. 1
- [44] Pierre Lebreton, Alexander Raake, Marcus Barkowsky, and Patrick Le Callet. Perceptual depth indicator for s-3d content based on binocular and monocular cues. In *Asilomar Conference on Signals, Systems and Computers*, 2012. 1, 3
- [45] Wei-Hong Li, Steven McDonagh, Ales Leonardis, and Hakan Bilen. Multi-task learning with 3d-aware regularization. In *ICLR*, 2024. 2
- [46] Jingyun Liang, Yuchen Fan, Kai Zhang, Radu Timofte, Luc Van Gool, and Rakesh Ranjan. Movidéo: Motion-aware video generation with diffusion models. In *ECCV*, 2024. 1
- [47] Drew Linsley, Peisen Zhou, Alekh Karkada Ashok, Akash Nagaraj, Gaurav Gaonkar, Francis E Lewis, Zygmunt Pizlo, and Thomas Serre. The 3d-pc: a benchmark for visual perspective taking in humans and machines. *arXiv:2406.04138*, 2024. 1, 3
- [48] Shichen Liu, Yichao Zhou, and Yajie Zhao. Vapid: A rapid vanishing point detector via learned optimizers. In *ICCV*, 2021. 4
- [49] Zhuang Liu, Hanzi Mao, Chao-Yuan Wu, Christoph Feichtenhofer, Trevor Darrell, and Saining Xie. A convnet for the 2020s. In *CVPR*, 2022. 5, 20, 21
- [50] Wufei Ma, Guofeng Zhang, Qihao Liu, Guanning Zeng, Adam Kortylewski, Yaoyao Liu, and Alan Yuille. Imagenet3d: Towards general-purpose object-level 3d understanding. In *NeurIPS*, 2024. 15
- [51] Yunze Man, Shuhong Zheng, Zhipeng Bao, Martial Hebert, Liang-Yan Gui, and Yu-Xiong Wang. Lexicon3d: Probing visual foundation models for complex 3d scene understanding. *arXiv:2409.03757*, 2024. 2
- [52] Octave Mariotti, Oisín Mac Aodha, and Hakan Bilen. Improving semantic correspondence with viewpoint-guided spherical maps. In *CVPR*, 2024. 8
- [53] Pushmeet Kohli Nathan Silberman, Derek Hoiem and Rob Fergus. Indoor segmentation and support inference from rgb-d images. In *ECCV*, 2012. 2
- [54] Thomas P O’Connell, Tyler Bonnen, Yoni Friedman, Ayush Tewari, Josh B Tenenbaum, Vincent Sitzmann, and Nancy Kanwisher. Approaching human 3d shape perception with neurally mappable models. *arXiv:2308.11300*, 2023. 3
- [55] Maxime Oquab, Timothée Darcet, Théo Moutakanni, Huy V. Vo, Marc Szafraniec, Vasil Khalidov, Pierre Fernandez, Daniel HAZIZA, Francisco Massa, Alaaeldin El-Nouby, Mido Assran, Nicolas Ballas, Wojciech Galuba, Russell Howes, Po-Yao Huang, Shang-Wen Li, Ishan Misra, Michael Rabbat, Vasu Sharma, Gabriel Synnaeve, Hu Xu, Herve Jegou, Julien Mairal, Patrick Labatut, Armand Joulin, and Piotr Bojanowski. DINOv2: Learning robust visual features without supervision. *TMLR*, 2024. 1, 2, 5, 12, 20, 21
- [56] J O’Keefe. The hippocampus as a cognitive map, 1978. 2
- [57] Alec Radford, Jong Wook Kim, Chris Hallacy, Aditya Ramesh, Gabriel Goh, Sandhini Agarwal, Girish Sastry, Amanda Askell, Pamela Mishkin, Jack Clark, et al. Learning transferable visual models from natural language supervision. In *ICML*, 2021. 1, 2, 5, 20, 21
- [58] Rishi Rajalingham, Elias B Issa, Pouya Bashivan, Kohitij Kar, Kailyn Schmidt, and James J DiCarlo. Large-scale, high-resolution comparison of the core visual object recognition behavior of humans, monkeys, and state-of-the-art deep artificial neural networks. *Journal of Neuroscience*, 2018. 3
- [59] René Ranftl, Katrin Lasinger, David Hafner, Konrad Schindler, and Vladlen Koltun. Towards robust monocular depth estimation: Mixing datasets for zero-shot cross-dataset transfer. *TPAMI*, 2020. 2, 5, 20, 21
- [60] René Ranftl, Alexey Bochkovskiy, and Vladlen Koltun. Vision transformers for dense prediction. In *ICCV*, 2021. 12
- [61] Robin Rombach, Andreas Blattmann, Dominik Lorenz, Patrick Esser, and Björn Ommer. High-resolution image synthesis with latent diffusion models. In *CVPR*, 2022. 1, 2, 5, 20, 21
- [62] Christoph Schuhmann, Romain Beaumont, Richard Vencu, Cade Gordon, Ross Wightman, Mehdi Cherti, Theo Coombes, Aarush Katta, Clayton Mullis, Mitchell Wortsman, et al. Laion-5b: An open large-scale dataset for training next generation image-text models. *NeurIPS*, 2022. 20

- [63] Nathan Silberman, Derek Hoiem, Pushmeet Kohli, and Rob Fergus. Indoor segmentation and support inference from rgb-d images. In *ECCV*, 2012. 5, 8, 12
- [64] Shuran Song, Samuel P Lichtenberg, and Jianxiong Xiao. Sun rgb-d: A rgb-d scene understanding benchmark suite. In *CVPR*, 2015. 3, 4, 17
- [65] Jaime Spencer, Chris Russell, Simon Hadfield, and Richard Bowden. Deconstructing self-supervised monocular reconstruction: The design decisions that matter. *TMLR*, 2022. 2
- [66] Jonas Theiner, Nils Nommensen, Jim Rhotert, Matthias Springstein, Eric Müller-Budack, and Ralph Ewerth. Analyzing results of depth estimation models with monocular criteria. In *CVPR Workshops*, 2023. 2
- [67] Xin Tong, Xianghua Ying, Yongjie Shi, Ruibin Wang, and Jinfan Yang. Transformer based line segment classifier with image context for real-time vanishing point detection in manhattan world. In *CVPR*, 2022. 4
- [68] Hugo Touvron, Matthieu Cord, and Hervé Jégou. Deit iii: Revenge of the vit. In *ECCV*, 2022. 5, 20, 21
- [69] Ruicheng Wang, Sicheng Xu, Cassie Dai, Jianfeng Xiang, Yu Deng, Xin Tong, and Jiaolong Yang. Moge: Unlocking accurate monocular geometry estimation for open-domain images with optimal training supervision. *arXiv preprint arXiv:2410.19115*, 2024. 17
- [70] Shuzhe Wang, Vincent Leroy, Yohann Cabon, Boris Chidlovskii, and Jerome Revaud. Dust3r: Geometric 3d vision made easy. In *CVPR*, 2024. 5, 20, 21
- [71] Tianyu Wang, Xiaowei Hu, Qiong Wang, Pheng-Ann Heng, and Chi-Wing Fu. Instance shadow detection. In *CVPR*, 2020. 3, 18
- [72] Philippe Weinzaepfel, Vincent Leroy, Thomas Lucas, Romain Brégier, Yohann Cabon, Vaibhav Arora, Leonid Antsfeld, Boris Chidlovskii, Gabriela Csurka, and Jérôme Revaud. Croco: Self-supervised pre-training for 3d vision tasks by cross-view completion. *NeurIPS*, 2022. 2, 5, 20, 21
- [73] Ross Wightman. Pytorch image models. <https://github.com/rwightman/pytorch-image-models>, 2019. 20
- [74] Thomas Wolf, Lysandre Debut, Victor Sanh, Julien Chaumond, Clement Delangue, Anthony Moi, Pierric Cistac, Tim Rault, Rémi Louf, Morgan Funtowicz, Joe Davison, Sam Shleifer, Patrick von Platen, Clara Ma, Yacine Jernite, Julien Plu, Canwen Xu, Teven Le Scao, Sylvain Gugger, Mariama Drame, Quentin Lhoest, and Alexander M. Rush. Transformers: State-of-the-art natural language processing. In *EMNLP System Demonstrations*, 2020. 20
- [75] Scott Workman, Menghua Zhai, and Nathan Jacobs. Horizon lines in the wild. In *BMVC*, 2016. 3, 5, 19
- [76] Saining Xie, Ross Girshick, Piotr Dollár, Zhuowen Tu, and Kaiming He. Aggregated residual transformations for deep neural networks. In *CVPR*, 2017. 5, 20, 21
- [77] Lihe Yang, Bingyi Kang, Zilong Huang, Xiaogang Xu, Jiashi Feng, and Hengshuang Zhao. Depth anything: Unleashing the power of large-scale unlabeled data. In *CVPR*, 2024. 2, 17
- [78] Lihe Yang, Bingyi Kang, Zilong Huang, Zhen Zhao, Xiaogang Xu, Jiashi Feng, and Hengshuang Zhao. Depth anything v2. *NeurIPS*, 2024. 1, 2, 5, 7, 20, 21
- [79] Yuanwen Yue, Anurag Das, Francis Engelmann, Siyu Tang, and Jan Eric Lenssen. Improving 2d feature representations by 3d-aware fine-tuning. In *ECCV*, 2024. 2, 5, 8
- [80] Xiaohua Zhai, Basil Mustafa, Alexander Kolesnikov, and Lucas Beyer. Sigmoid loss for language image pre-training. In *ICCV*, 2023. 5, 20, 21
- [81] Guanqi Zhan, Chuanxia Zheng, Weidi Xie, and Andrew Zisserman. A general protocol to probe large vision models for 3d physical understanding. In *NeurIPS*, 2024. 1, 2, 4, 5, 15
- [82] Lvmin Zhang, Anyi Rao, and Maneesh Agrawala. Adding conditional control to text-to-image diffusion models. In *ICCV*, 2023. 1
- [83] Xiaoshuai Zhang, Zhicheng Wang, Howard Zhou, Soham Ghosh, Danushen Gnanapragasam, Varun Jampani, Hao Su, and Leonidas Guibas. ConDense: Consistent 2d/3d pre-training for dense and sparse features from multi-view images. In *ECCV*, 2024. 2
- [84] Jinghao Zhou, Chen Wei, Huiyu Wang, Wei Shen, Cihang Xie, Alan Yuille, and Tao Kong. ibot: Image bert pre-training with online tokenizer. *ICLR*, 2022. 5, 20, 21
- [85] Tinghui Zhou, Matthew Brown, Noah Snavely, and David G Lowe. Unsupervised learning of depth and ego-motion from video. In *CVPR*, 2017. 2
- [86] Zihan Zhou, Farshid Farhat, and James Z Wang. Detecting dominant vanishing points in natural scenes with application to composition-sensitive image retrieval. *Transactions on Multimedia*, 2017. 3, 4
- [87] Chenming Zhu, Tai Wang, Wenwei Zhang, Jiangmiao Pang, and Xihui Liu. LLaVA-3D: A simple yet effective pathway to empowering LMMs with 3d-awareness. *arXiv:2409.18125*, 2024. 7
- [88] Yan Zhu, Yuandong Tian, Dimitris Metaxas, and Piotr Dollár. Semantic amodal segmentation. In *CVPR*, 2017. 3, 4, 16, 18

Appendix

A. Additional Results on *DepthCues*

A.1. Full Benchmark Results

In the main paper, we reported the performance of 20 pre-trained vision models on *DepthCues* and NYUv2 [63] using bar charts, and focused on salient observations. Here we provide detailed numerical results on these datasets and additionally the linear probing results on ImageNet-1k [14]. Moreover, we also provide an analysis of the impact of the pre-training dataset, objective, and architectural choices of the vision models on their performance. Our analysis is based solely on publicly available models; therefore, as outlined in the limitations section of the main paper, we are unable to control all variables in these analyses.

The probing results of all models are summarized in Tab. A1, and the average performance of models on *DepthCues* is plotted against their NYUv2 depth estimation results in Fig. A1. It is noted that there are slight differences between the linear probing results on NYUv2 and ImageNet-1k compared to previous works [17, 55]. These may stem from differences in the implementation details including the features probed, learning rates, and training iterations, *etc.* For example, the probing results on NYUv2 depth estimation in [17] are generally higher than our results. Possible reasons for this include the following factors. Firstly, while we train a simple linear layer to probe the patch tokens from the last layer of the vision models, a more complex non-linear probe similar to the DPT decoder [60] is used to probe features from multiple layers of the models in [17]. Secondly, the class tokens are utilized for several models (*e.g.*, DINO, DINOv2) in [17], while we only use patch tokens for consistent evaluation across all models as some of the models do not include a class token. Thirdly, because of the difference in the probes, their optimization hyper-parameters can differ. Similar reasons can be applied to the differences in our ImageNet-1k probing results from previous works. In particular, for CLIP, the class token seems to be crucial for its ImageNet classification ability. We made these design choices because our primary focus is to evaluate the awareness of human-like monocular depth cues in vision models in a fair and comparable manner, rather than optimizing their probing performance on external benchmarks.

Impact of Pre-Training Dataset Size. Fig. A2 shows the average performance of models on *DepthCues* against the size of their pre-training datasets. Excluding two vision-language models (CLIP and SigLIP) and the generative model (StableDiffusion, which also trained for text-to-image generation using language supervision), there is a moderate positive correlation between these two variables (Pearson’s $r = 0.69, p = 0.002$). Apart from the overall

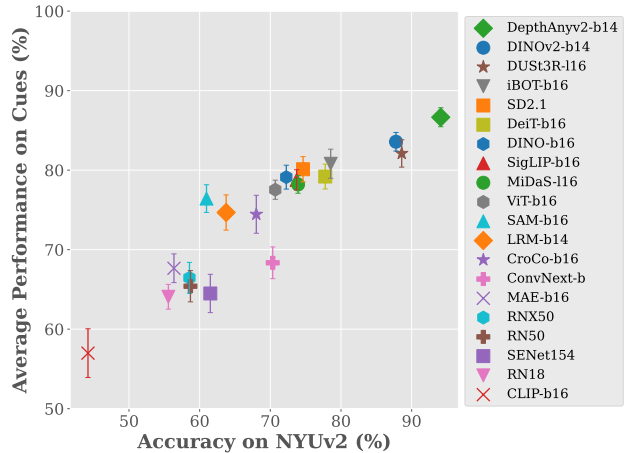


Figure A1. **Performance of vision models on *DepthCues* vs. NYUv2 depth estimation.** A strong correlation is observed between depth cue understanding and depth estimation.

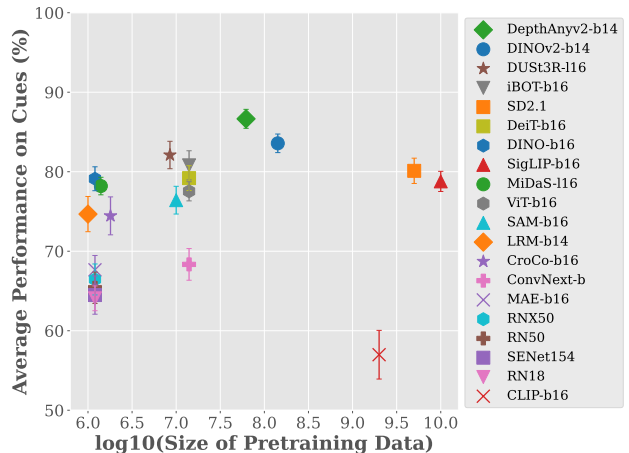


Figure A2. **Impact of pre-training dataset size on the performance of vision models on *DepthCues*.** Omitting the three models that involve language supervision (CLIP, SigLIP, and SD), we observe a moderate positive correlation between depth cue understanding and pre-training data size.

trend, we observe that certain models demonstrate greater data efficiency in developing depth cue awareness. For instance, among models pre-trained on approximately 10^6 data samples, DINO achieves the best performance. For those pre-trained on around 10^7 samples, DUST3R emerges as the best. Finally, when comparing models pre-trained on roughly one order of magnitude more data, DepthAnythingv2 outperforms DINOv2. However, there are other factors such as the pre-training objective, model architecture, and the dataset distribution which can confound these analyses. It is desirable to perform future studies on the pre-training dataset size where the aforementioned factors are better controlled.

	<i>DepthCues</i>						NYUv2	ImageNet-1k
	elevation (%)	light-shadow (%)	occlusion (%)	perspective (%)	size (%)	texture-grad (%)	depth (%)	classification (%)
CLIP-b16	27.56 (2.76)	62.49 (0.19)	58.41 (0.20)	58.40 (3.06)	68.37 (0.21)	66.68 (0.77)	44.20	0.59
RN18	57.17 (0.83)	61.86 (0.84)	72.79 (0.20)	53.87 (3.97)	70.57 (0.11)	68.22 (0.35)	55.57	68.67
SENet154	55.19 (2.97)	60.95 (1.04)	74.07 (0.09)	47.47 (2.71)	76.94 (0.63)	72.30 (0.32)	61.51	81.58
RN50	58.38 (1.61)	61.26 (0.48)	75.96 (0.18)	52.53 (3.05)	76.01 (1.35)	68.26 (1.00)	58.70	73.62
RNX50	59.72 (1.73)	62.49 (0.82)	76.36 (0.20)	52.93 (5.07)	75.93 (0.77)	71.28 (0.07)	58.56	76.40
MAE-b16	51.03 (3.33)	75.72 (0.99)	68.05 (0.22)	66.93 (3.23)	74.27 (1.40)	69.96 (0.66)	56.36	25.99
ConvNext-b	62.52 (1.21)	61.86 (0.64)	75.60 (0.22)	55.07 (6.52)	79.04 (0.47)	75.98 (0.50)	70.34	80.37
CroCo-b16	56.64 (1.57)	78.28 (0.66)	69.21 (0.08)	74.53 (4.57)	75.64 (0.72)	92.40 (0.14)	68.02	14.52
LRM-b14	56.58 (1.75)	76.56 (0.68)	69.14 (0.02)	83.07 (5.79)	75.51 (0.97)	87.18 (0.51)	63.75	17.68
SAM-b16	62.33 (1.56)	74.93 (0.70)	78.29 (0.10)	89.07 (1.16)	76.74 (0.49)	77.18 (0.43)	60.97	19.58
ViT-b16	71.68 (1.57)	74.42 (0.50)	73.94 (0.06)	87.60 (2.09)	76.29 (1.42)	81.28 (0.23)	70.70	68.67
MiDaS-116	71.04 (1.38)	77.70 (0.66)	74.02 (0.16)	84.93 (6.29)	77.70 (2.27)	83.80 (0.50)	73.93	42.79
SigLIP-b16	71.44 (4.12)	76.98 (0.53)	77.76 (0.08)	89.60 (3.64)	81.40 (1.10)	75.52 (0.13)	73.73	37.96
DINO-b16	73.80 (3.15)	75.19 (0.29)	72.63 (0.18)	91.20 (0.78)	76.88 (0.40)	85.00 (0.54)	72.26	41.29
DeiT-b16	67.44 (1.26)	79.81 (0.41)	78.00 (0.12)	91.47 (1.66)	78.17 (0.92)	80.28 (0.37)	77.77	84.53
SD2.1	69.45 (3.56)	78.53 (0.26)	78.20 (0.14)	93.07 (1.00)	77.92 (1.85)	83.50 (0.74)	74.63	32.67
iBOT-b16	72.08 (1.32)	76.05 (0.50)	75.19 (0.09)	96.67 (1.58)	79.61 (0.89)	85.24 (0.34)	78.54	38.92
DUST3R-116	74.65 (2.44)	76.75 (0.45)	76.02 (0.30)	95.47 (0.98)	80.31 (0.92)	89.42 (0.35)	88.59	25.94
DINOv2-b14	79.13 (1.11)	83.95 (0.25)	79.93 (0.17)	94.53 (1.86)	83.57 (0.93)	80.32 (0.49)	87.78	77.95
DepthAnyv2-b14	83.74 (0.57)	84.74 (0.68)	81.01 (0.08)	96.93 (0.90)	83.51 (1.59)	89.98 (0.34)	94.12	68.67

Table A1. **Detailed evaluation results on *DepthCues*, depth estimation (NYUv2), and image classification (ImageNet-1k).** The mean and standard deviation of the accuracy of each vision model on the six tasks in our benchmark are summarized. The last two columns show the accuracy of these models on NYUv2 depth estimation and ImageNet-1k classification.

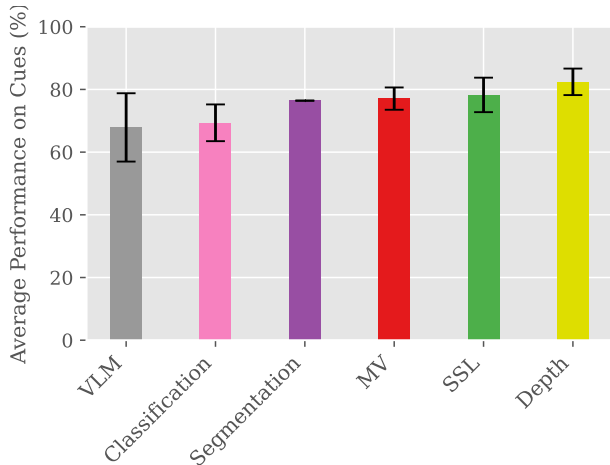


Figure A3. **Average performance of vision models on *DepthCues* by pre-training objective.** The error bar denotes the standard deviation over models.

Impact of Pre-Training Objective. We report the average performance achieved on *DepthCues* by models pre-trained with different types of supervision in Fig. A3. On average, models pre-trained for depth estimation obtain the highest performance, followed by (single-view) self-supervised (SSL) and multi-view models. Considering the differences in the pre-training data of these groups, we also collate results for different groups when the pre-training dataset is the same. The only models that support such analysis are either classification or SSL-based (more details in Appendix D), and their results are shown in Fig. A4. We can

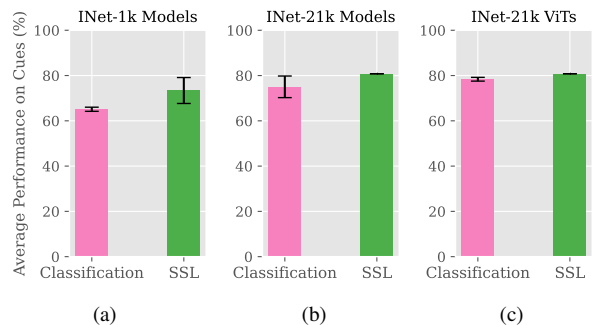


Figure A4. **Average performance of vision models on *DepthCues* by pre-training objective, with fixed pre-training data.** We show results for ImageNet-1k (a) and ImageNet-21k models (b), and ImageNet-21k ViT-based models (c). The error bar denotes the standard deviation over models.

see from Fig. A4 (a) and (b) that SSL methods have developed a better understanding of studied depth cues on average. However, in these two plots, the architecture of classification models is mixed (convolutional and transformer-based models), whereas SSL models only contain ViT backbones. Therefore, we further reduce the effect of architecture and show a comparison for ViT-only models (‘Base’ models; patch size 16) in Fig. A4 (c), where we still see an advantage from the SSL model (iBOT) over the classification ones (ViT and DeiT).

Impact of Model Architecture. Here we compare the average depth cue awareness between vision transformer (ViT)-based models and models with convolutional architectures

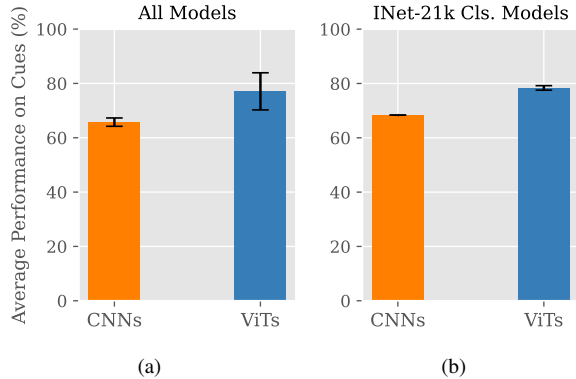


Figure A5. **Average performance of vision models on *DepthCues* by model architecture.** We show results for all models (a) and ImageNet-21k classification models (b). The error bar denotes the standard deviation over models.

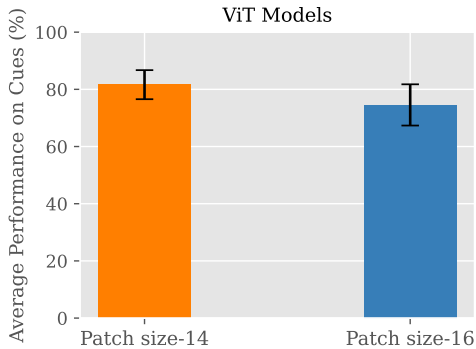


Figure A6. **Average performance of ViT-based models on *DepthCues* by patch size.** The error bar denotes the standard deviation over models.

(CNNs). Fig. A5 (a) shows the results for all evaluated models, regardless of pre-training objective and dataset, where we see a clear advantage of the ViT models. To reduce confounding factors, in Fig. A5 (b) we also compare these architectures when the pre-training setting is fixed to be classification on ImageNet-21k. It is observed that under such a setting, the two ViT models (ViT and DeiT) demonstrate enhanced knowledge of depth cues compared to ConvNext. **Impact of Patch Size on ViT Models.** We also perform a comparison between ViT models regarding their patch size. As shown in Fig. A6, models with a smaller patch size (14 vs. 16) achieved better average performance on *DepthCues*. However, it is noted that the “patch size-14” models only include DINOv2, DepthAnythingv2, and LRM, and there may be other factors that led to their superior performance.

A.2. Comparison Between Probes

As discussed in Sec. 4.2 in the main paper, we adopt non-linear probes to evaluate models on *DepthCues*. Specifically, an MLP probe is used for light-shadow, occlusion, size, and texture-grad, and an attentive probe [5, 18] is used

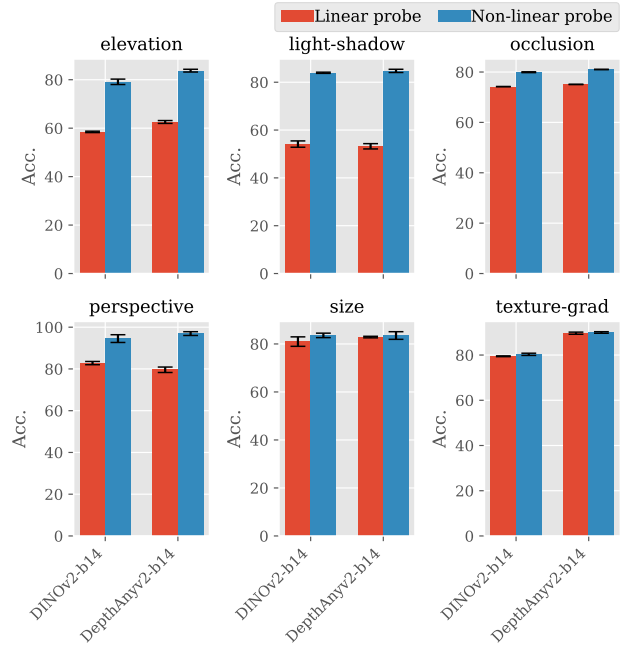


Figure A7. **Linear vs. non-linear probes.** We see consistently better performance from non-linear probes across the tasks in *DepthCues*.

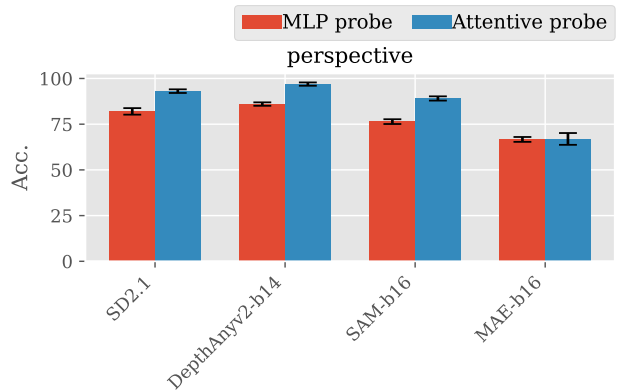


Figure A8. **MLP vs. Attentive probe on the perspective task.** We observe that for a task that requires global information, the attentive probe yields better results than an MLP.

for elevation and perspective. Our motivation for using these instead of linear probes is that it is not clear that the solutions to our tasks should be a linear function of the model features. In addition, non-linear probes have been adopted in previous work on probing vision models for depth estimation [17, 22]. To justify our choice empirically, we compare our non-linear probes and the linear probe. Following the same protocol described in the main paper, we obtained additional linear probing results of two models (DINOv2 and DepthAnythingv2) on all six depth cue tasks. The results are summarized in Fig. A7, showing that our non-

Model	Layers Probed	Elevation (%)				Light-shadow (%)				Occlusion (%)			
		Block 1	Block 2	Block 3	Block 4	Block 1	Block 2	Block 3	Block 4	Block 1	Block 2	Block 3	Block 4
CLIP-b16	{3, 6, 9, 12}	0.189	0.243	0.372	0.355	66.357	64.965	65.893	65.429	58.283	57.531	55.912	56.206
RN18	{1, 2, 3, 4}	0.145	0.127	0.122	0.105	64.965	63.805	65.197	65.029	58.360	67.302	73.175	66.744
SENet154	{1, 2, 3, 4}	0.120	0.108	0.105	0.112	65.893	66.357	66.473	67.749	60.987	74.066	73.532	68.681
RN50	{1, 2, 3, 4}	0.138	0.118	0.096	0.109	65.197	65.429	65.313	69.026	59.391	65.737	75.701	70.735
RNX50	{1, 2, 3, 4}	0.136	0.113	0.097	0.113	65.777	65.545	66.357	68.329	59.329	69.913	76.554	67.480
MAE-b16	{3, 6, 9, 12}	0.151	0.130	0.116	0.122	81.323	81.787	82.251	80.510	61.623	63.381	67.550	66.744
ConvNext-b	{1, 2, 3, 4}	0.129	0.121	0.108	0.096	65.197	66.125	69.722	67.169	59.623	65.838	75.136	71.347
CroCo-b16	{3, 6, 9, 12}	0.125	0.111	0.107	0.108	83.411	83.991	83.759	83.411	62.870	65.946	68.712	68.271
LRM-b14	{3, 6, 9, 12}	0.135	0.108	0.108	0.114	68.677	81.903	84.919	83.411	62.142	67.651	69.650	67.256
SAM-b16	{3, 6, 9, 12}	0.133	0.111	0.085	0.084	80.046	80.858	80.046	80.278	63.513	72.571	78.080	78.700
ViT-b16	{3, 6, 9, 12}	0.101	0.081	0.087	0.098	79.466	81.671	76.798	70.186	64.637	72.393	73.291	67.883
MiDaS-116	{6, 12, 18, 24}	0.108	0.078	0.091	0.083	83.759	80.974	79.814	78.886	69.882	73.524	73.408	73.222
SigLIP-b16	{3, 6, 9, 12}	0.090	0.072	0.072	0.083	80.858	86.543	81.903	71.694	68.852	76.809	74.508	70.277
DINO-b16	{3, 6, 9, 12}	0.099	0.073	0.073	0.074	81.206	82.483	83.179	81.903	65.791	72.641	73.470	73.617
DeiT-b16	{3, 6, 9, 12}	0.091	0.084	0.086	0.118	83.527	87.007	73.434	66.357	68.681	77.158	73.679	67.488
SD2.1	{1, 2, 3, 4}	0.100	0.094	0.096	0.139	81.090	88.399	79.698	66.125	69.371	77.096	72.129	59.468
iBOT-b16	{3, 6, 9, 12}	0.114	0.093	0.081	0.078	78.190	82.947	83.527	83.527	62.994	72.772	75.027	73.570
DUSi3R-116	{18, 24, 33, 36}	0.066	0.076	0.083	0.093	83.759	86.427	85.383	82.251	73.764	69.975	74.330	75.833
DINOv2-b14	{3, 6, 9, 12}	0.117	0.073	0.068	0.065	67.053	79.234	89.211	87.935	63.412	76.399	79.544	75.205
DepthAnyv2-b14	{3, 6, 9, 12}	0.114	0.070	0.064	0.058	66.473	79.350	90.603	90.023	63.436	77.111	80.962	77.057

Model	Layers Probed	Perspective (%)				Size (%)				Texture-grad (%)			
		Block 1	Block 2	Block 3	Block 4	Block 1	Block 2	Block 3	Block 4	Block 1	Block 2	Block 3	Block 4
CLIP-b16	{3, 6, 9, 12}	0.259	0.230	0.253	0.264	73.636	73.635	72.727	70.909	67.000	64.900	63.600	61.200
RN18	{1, 2, 3, 4}	0.290	0.265	0.235	0.259	68.485	78.788	77.273	77.273	67.400	65.300	64.500	63.700
SENet154	{1, 2, 3, 4}	0.270	0.250	0.262	0.294	74.242	77.879	83.333	81.515	69.200	74.800	66.300	64.400
RN50	{1, 2, 3, 4}	0.296	0.290	0.230	0.264	73.030	75.455	78.788	78.485	68.500	69.000	70.200	67.300
RNX50	{1, 2, 3, 4}	0.294	0.270	0.240	0.277	70.606	78.182	80.606	76.061	68.900	72.600	69.000	65.200
MAE-b16	{3, 6, 9, 12}	0.264	0.240	0.218	0.217	76.364	79.697	79.696	78.485	66.300	69.500	68.900	69.800
ConvNext-b	{1, 2, 3, 4}	0.291	0.296	0.244	0.248	71.818	74.242	80.303	81.818	70.800	73.600	61.600	63.600
CroCo-b16	{3, 6, 9, 12}	0.234	0.177	0.148	0.153	76.364	77.273	79.091	78.788	74.900	89.800	91.600	92.700
LRM-b14	{3, 6, 9, 12}	0.253	0.200	0.146	0.137	75.152	78.485	80.000	79.697	66.900	72.900	81.000	87.800
SAM-b16	{3, 6, 9, 12}	0.224	0.178	0.116	0.145	76.667	80.909	80.606	80.909	76.800	78.200	74.600	71.800
ViT-b16	{3, 6, 9, 12}	0.149	0.109	0.108	0.213	77.879	79.394	80.000	78.788	75.100	82.600	76.000	70.100
MiDaS-116	{6, 12, 18, 24}	0.227	0.135	0.137	0.158	76.970	78.788	77.879	78.485	84.100	85.200	84.000	83.300
SigLIP-b16	{3, 6, 9, 12}	0.181	0.111	0.124	0.161	79.091	81.515	79.697	82.121	76.700	78.300	69.700	61.700
DINO-b16	{3, 6, 9, 12}	0.152	0.078	0.092	0.115	77.576	80.303	77.576	79.091	80.000	84.700	84.900	84.000
DeiT-b16	{3, 6, 9, 12}	0.179	0.107	0.194	0.251	77.576	80.909	80.303	80.606	79.900	81.100	72.100	62.500
SD2.1	{1, 2, 3, 4}	0.102	0.110	0.105	0.297	79.091	81.212	79.091	73.636	81.800	83.200	79.600	70.300
iBOT-b16	{3, 6, 9, 12}	0.182	0.086	0.069	0.078	79.091	80.909	79.697	81.818	80.400	83.600	85.100	84.200
DUSi3R-116	{18, 24, 33, 36}	0.076	0.097	0.098	0.106	83.636	85.455	82.121	77.576	87.500	87.600	91.700	91.900
DINOv2-b14	{3, 6, 9, 12}	0.218	0.142	0.089	0.088	79.091	79.697	82.727	85.455	77.200	82.500	80.800	80.600
DepthAnyv2-b14	{3, 6, 9, 12}	0.189	0.091	0.085	0.092	77.576	83.030	82.424	86.667	76.700	83.000	86.100	90.000

Table A2. **Layer search for all models on all tasks in *DepthCues*.** We report the validation performance of different layers, and **bold** the best score for each model. Note that “Block i ” corresponds to the i th layer indicated in the second column. Horizon detection error and Euclidean distance are used to assess validation performance for elevation and perspective respectively, while accuracy is used for the other four tasks.

linear probes consistently outperform linear probes, based on the average of five runs, although the gap is small for size and texture-grad. Moreover, for the light-shadow task, the performance of the linear probe is close to random, indicating that a linear classifier is not sufficient to solve the problem using these models’ features.

For elevation and perspective, our choice of the attentive probe, instead of the MLP probe used for the other four tasks, is motivated by the extra step in the former for aggregating global information, which we consider important for these two tasks. This is also supported by our results in Fig. A8, where it can be seen that the attentive probe results in significant performance gains for most models on

the perspective task.

A.3. Hyper-Parameter Search Results

It has been shown in previous works [50, 81] that different layers of pre-trained vision models have varied performance when probed for different tasks. Therefore, for all the 20 vision models, we perform a hyper-parameter search on their layers. We restrict the search to four layers for each model, which are selected by equally dividing the networks into four blocks (similar to [17]), where applicable. We train the probes on features from each block, and evaluate their validation performance. The layer with the best validation result is then selected for subsequent analysis. The layer













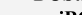




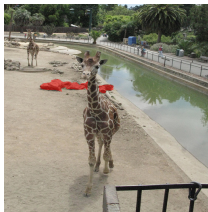

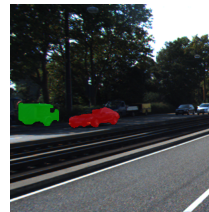


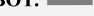











 Elevation	 Light-shadow	 Occlusion	 Perspective	 Size	 Texture-grad
Task: Horizon line estimation.	Task: Is object A assoc. w/ shadow B ?	Task: Is object A occluded?	Task: Vanishing point estimation.	Task: Is object A larger than B ?	Task: Is region A closer than B ?
					
GT:  DepthAnyv2:  DINOv2:  DUS3R:  iBOT:  SD: 	GT:  DepthAnyv2:  DINOv2:  DUS3R:  iBOT:  SD: 	GT:  DepthAnyv2:  DINOv2:  DUS3R:  iBOT:  SD: 	GT:  DepthAnyv2:  DINOv2:  DUS3R:  iBOT:  SD: 	GT:  DepthAnyv2:  DINOv2:  DUS3R:  iBOT:  SD: 	GT:  DepthAnyv2:  DINOv2:  DUS3R:  iBOT:  SD: 
					
GT:  DepthAnyv2:  DINOv2:  DUS3R:  iBOT:  SD: 	GT:  DepthAnyv2:  DINOv2:  DUS3R:  iBOT:  SD: 	GT:  DepthAnyv2:  DINOv2:  DUS3R:  iBOT:  SD: 	GT:  DepthAnyv2:  DINOv2:  DUS3R:  iBOT:  SD: 	GT:  DepthAnyv2:  DINOv2:  DUS3R:  iBOT:  SD: 	GT:  DepthAnyv2:  DINOv2:  DUS3R:  iBOT:  SD: 
(a)	(b)	(c)	(d)	(e)	(f)

Figure A9. Failure cases of the top-five vision models on *DepthCues*. Each column shows two examples for a depth cue.

search results for all models are summarized in Tab. A2. Consistent with previous findings, we observe that different layers of a model exhibit varying strengths. For instance, in DINOv2, the 9th layer achieved the best performance on light-shadow and occlusion, the 12th layer provides superior features for elevation, perspective, and size, while texture-grad is handled best by the 6th layer.

A.4. Example Model Failure Cases

We examine where vision models consistently fail. Focusing on the top-five models, namely DepthAnythingv2, DINOv2, DUS3R, iBOT, and StableDiffusion, we identify test instances where they all fail to predict the correct label over five runs, and visualize these cases in Fig. A9.

Elevation. In the first (top row) instance of Fig. A9 (a), the horizon line is largely occluded by the architectures, making it a challenging case. In the second case (bottom row), although the horizon line is less occluded by objects, its visibility is still low due to the fog, which can be a possible

explanation for the failure of the models.

Light-shadow. In both of the examples in Fig. A9 (b), the target objects (overlaid with red masks) and query shadows (overlaid with green masks) overlap with each other, possibly affecting the models’ predictions. This is especially the case for the second image, where the true shadow of the target object also overlaps with the false query shadow.

Occlusion. The first example (top row) of Fig. A9 (c) is challenging because the person highlighted with a red mask undergoes only very minor occlusion, limited to his feet. In the second example, the stones are treated as one object and labeled occluded in the source data [88], which can be confused with their individual boundaries or occlusions.

Perspective. Both of the examples in Fig. A9 (d) contain distractors that weaken the notion of the dominant vanishing point. In the first example (top), while the ground-truth label indicates the converging point of the two sides of the staircase, some models are influenced by the parallel lines formed by the bricks on the walls. In the second example

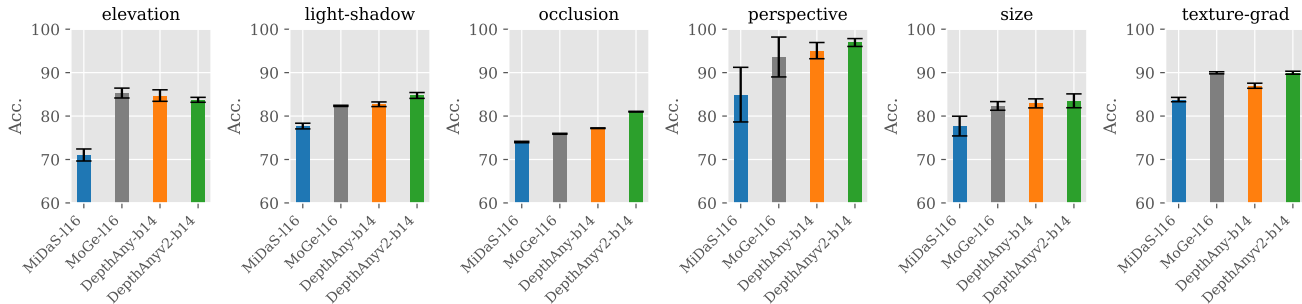


Figure A10. **Performance of monocular depth estimation models on *DepthCues*.** Here we evaluate recent depth estimation models, and observe that these models show competitive performance, indicating their strong understanding of the monocular depth cues.

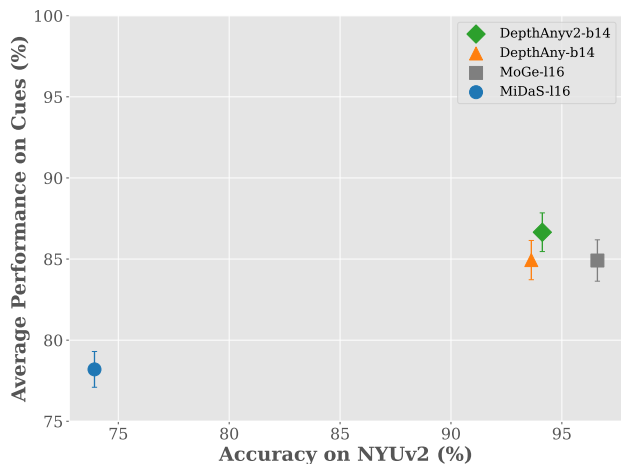


Figure A11. **Performance on monocular depth estimation models *DepthCues* vs. NYUv2 depth estimation.**

(bottom), some models might be affected by the intersection line of the mountain and sky.

Size. In the first example of Fig. A9 (e), all models incorrectly predicted that the car (highlighted in red) has a larger 3D size than the van (highlighted in green). In the second example, while the trailer (green) has a smaller size than the car, all models predicted the opposite case. These indicate limitations in the models’ understanding of the size cue.

Texture-grad. All models failed to predict the correct depth order in both cases in Fig. A9 (f). In these challenging images, the texture gradient cue is relatively weak, and the locations of the two regions are not drastically different, which can make these cases challenging.

A.5. Learning Depth Cues

In Sec. 5.2 of the main paper, we presented linear probing results on NYUv2 and DIW, showing that fine-tuning on *DepthCues* improves models’ performance on depth estimation. Here we further investigate whether the fine-tuned model has improved understanding of the depth cues by comparing the probing results of the fine-tuned and pre-

	<i>DepthCues</i> (%)					
	elevation	light-shadow	occlusion	perspective	size	texture-grad
DINOv2	77.46	83.26	75.35	96.00	83.57	78.90
DINOv2+DC	79.84 (+2.38)	82.67 (-0.59)	76.11(+0.76)	94.00 (-2.00)	86.10 (+2.53)	88.30 (+9.40)

Table A3. **Probing results of the original and fine-tuned DINOv2 on *DepthCues*.** Here ‘+DC’ indicates the fine-tuned model. We observe an overall increase in performance, especially on texture-grad.

trained DINOv2 on *DepthCues*. Note we focus on probing the last layer since LoRA was only applied on that layer during fine-tuning. The results from Tab. A3 shows that the fine-tuned version outperforms the original DINOv2 on four cues, with a slight drop in performance on light-shadow and perspective. Notably, we see a 9.4% increase in accuracy on texture-grad, on which the original DINOv2 shows relatively weaker understanding (see Fig. 3 in the main paper).

A.6. Monocular Depth Estimation Models

In addition to the 20 vision models evaluated in the main paper, here we present additional results for some recent monocular depth estimation models: DepthAnything [77] and MoGe [69]. The average performance of these models on *DepthCues* and depth estimation is shown in Fig. A10 and Fig. A11, along with the two depth models already included in our study. In general, we observe a similar trend to our previous findings, that the models’ depth estimation performance highly correlates with their performance on *DepthCues*.

B. Dataset Construction Details

Here we provide additional details on the construction of the *DepthCues* benchmark and show other examples from the datasets.

Instance Selection for Size. To create an instance for the size dataset, we sample two objects from an image, and obtain the label by comparing the volumes of their 3D bounding boxes (provided by the source datasets, KITTI [23] and SUN-RGBD [64]). It is mentioned in the main paper that a

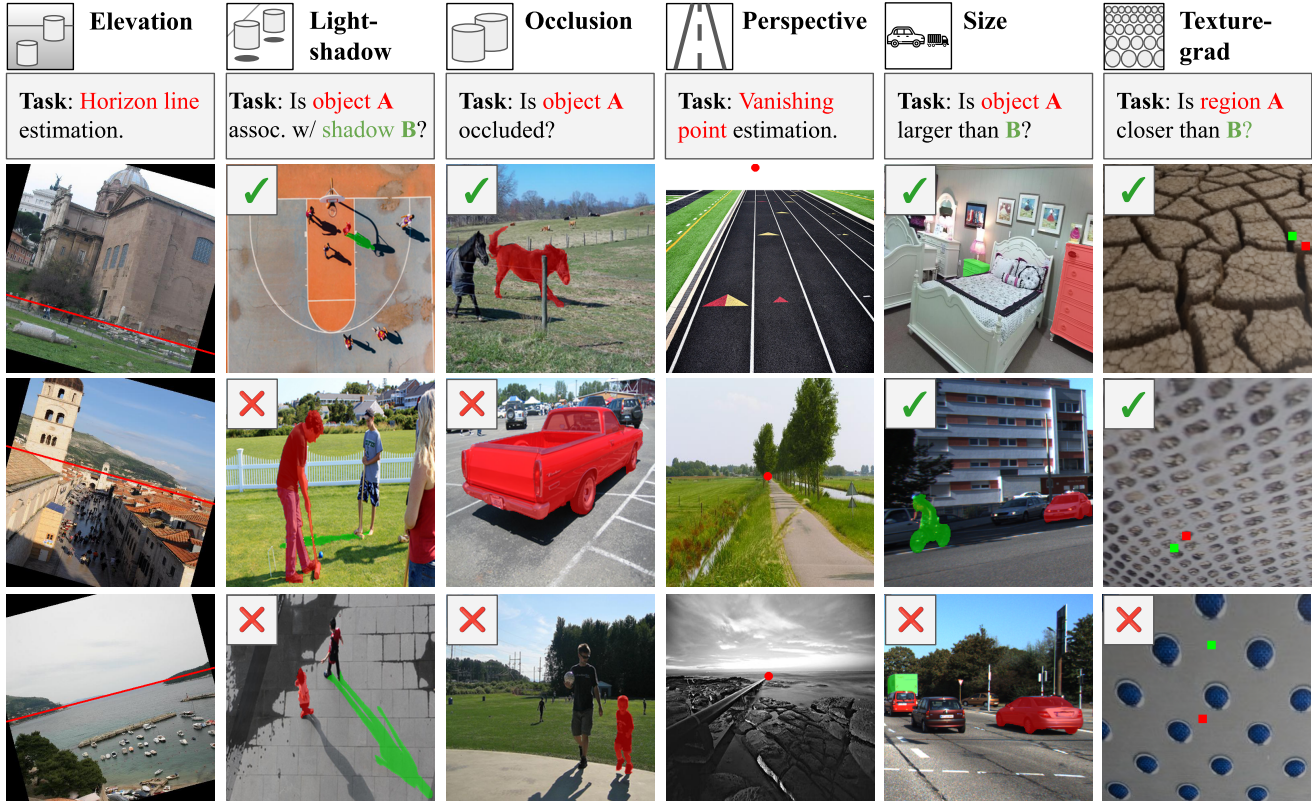


Figure A12. **Examples data instances from *DepthCues*.** The horizon lines for elevation and the vanishing points for perspective are indicated by red lines and dots respectively. For the other four cues where we define binary classification tasks, the labels are indicated by the ticks and crosses.

threshold is applied to filter out cases where the difference in the sizes of the two objects is very small. This is motivated by our observation that the 3D bounding boxes from the source datasets can contain minor errors. Therefore, to reduce mislabeling in the size dataset, we apply a minimum threshold of $2.5 m^3$ for the size difference between two objects in an image from KITTI, and a threshold of $0.4 m^3$ for SUN-RGBD. We found empirically that these thresholds provided a good balance between label accuracy and dataset size.

Generating Masks with SAM. Four of the tasks in *DepthCues*, namely light-shadow, occlusion, size, and texture-grad, require object masks for the probing evaluation. The object masks for light-shadow and occlusion are directly obtained from their source datasets [71, 88], and the masks for texture-grad are manually defined during dataset synthesis (see Sec. 3.6 in the main paper). However, the object masks for the size task are not available in the source datasets which are originally designed for 3D object detection. Therefore, we made use of an off-the-shelf segmentation model, SAM [41], to create these masks. Specifically, for each object, we obtain its 2D bounding box from the source dataset, and discard the object if its 2D bounding box has a height/width less than eight pixels, to filter

out potentially incorrect annotations. Next, we predict the mask for an object by feeding its 2D bounding box and the image to SAM, and only keep the part of the mask that falls into the 2D bounding box. Finally, to make sure the desired object is segmented, we check whether the mask takes up a too small portion of the bounding box ($< 20\%$), and discard the object if that is the case. These filtering steps are applied to both objects in a candidate image, and the candidate is included in the dataset only if both object masks pass these checks (and satisfy the size difference threshold specified above).

More Examples from the Datasets. Additional examples from the *DepthCues* datasets are shown in Fig. A12.

C. Additional Implementation Details

C.1. Probing Experiments

Probing Method. To evaluate vision models on *DepthCues*, we adopt a probing approach. While the task-specific feature extraction procedure and the probe models have been discussed in the paper, we illustrate the processes in Fig. A13.

Training Settings. The MLP probes for light-shadow, occlusion, size, and texture-grad are trained with a binary

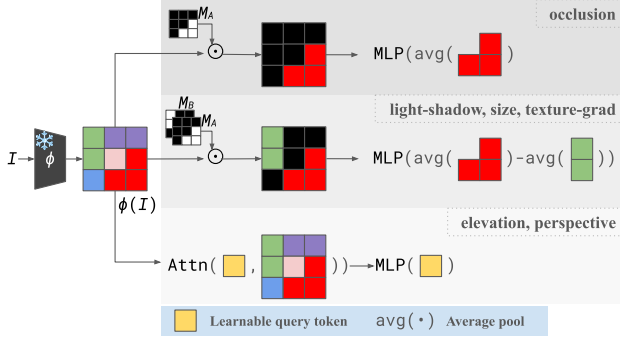


Figure A13. **Method for probing vision models on *DepthCues*.** We extract task-specific features from the image I using the vision model $\phi(\odot)$ and object masks where applicable, then train the MLP or attentive probe to solve the tasks in *DepthCues*. For illustrative purposes, here we only show 3×3 image features, but in practice, the spatial resolution is much higher.

cross-entropy loss since the associated tasks are binary classification ones. The attentive probes for elevation and perspective are trained with mean squared error loss due to their regression nature. All the MLP probes (for all tasks and all models) are trained for approximately 30k iterations with a batch size of eight, and the attentive probes are trained for 3,750 iterations with a batch size of 64. We used the AdamW [40] optimizer with cosine learning rate decay. For the hyperparameter search over model layers, we follow [17] and partition the networks into four equal-sized chunks, and evaluate the features from each chunk. For example, for DINOv2-b14, we search over layers 3, 6, 9, and 12.

Computational Cost. We provide an estimation of the computational cost for evaluating a model based on the ViT-Base architecture on *DepthCues*, using the standard implementation¹ of DINO [10]. Based on the statistics of our experiment runs, on a single NVIDIA RTX A5000 GPU (24GB VRAM), benchmarking a ViT-Base on *DepthCues* under our protocol and settings takes approximately 241 hours. This includes 92.7 hours for searching for the best layer for each cue (24 training + validation runs: 6 cues \times 4 layers), and 148.3 hours for repeating the probing of the best layer (30 training + test runs: 6 cues \times 5 repeats for statistical robustness). Note, these timings assume that the selected layer is the last one (*i.e.*, layer 12 for a ViT-Base model), and the total time can be lower than the estimate if this is not the case and the model is truncated up to the desired layer.

C.2. Evaluation Metrics

While we use accuracy to evaluate performance on the binary classification tasks, as discussed in the main paper we apply thresholding to the Euclidean distance (for perspec-

¹<https://github.com/facebookresearch/dino>.

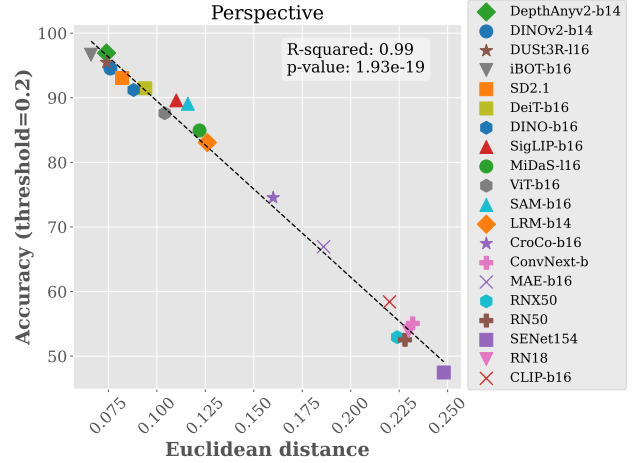


Figure A14. **Validating the threshold for evaluation of perspective.** We used a threshold of 0.2 to convert the Euclidean distance between ground-truth and predicted vanishing points to accuracy.

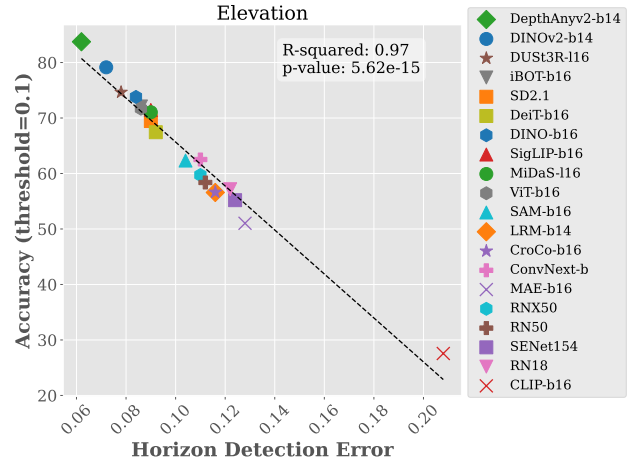


Figure A15. **Validating the threshold for evaluation of elevation.** We used a threshold of 0.1 to convert the horizon detection error to accuracy.

tive) and horizon detection error² [75] (for elevation) to convert these metrics into accuracy. Specifically, we used a threshold of 0.2 for perspective and 0.1 for elevation. We validate these choices of thresholds by evaluating the correlation between the original metrics and converted accuracies in Figs. A14 and A15.

For evaluation of depth estimation on NYUv2, as in [6, 17], we use accuracy, which is calculated per image using the ground-truth and predicted depth maps, d, \hat{d} , as:

$$\text{Acc} = \frac{1}{N} \sum_{i=1}^N \max\left(\frac{\hat{d}_i}{d_i}, \frac{d_i}{\hat{d}_i}\right) < 1.25, \quad (3)$$

²This measures the maximum distance between the predicted and the ground-truth horizon lines, normalized by the image height.

where N denotes the number of pixels in the image. For evaluation on DIW [11], we report the Weighted Human Disagreement Rate (WHDR), which measures the proportion of depth order predictions that disagree with the manual labels provided in DIW.

C.3. Fine-Tuning on *DepthCues*

To fine-tune the vision models on *DepthCues* we use Low Rank Adaptation (LoRA) [34]. Here, we specify our implementation for the fine-tuned models for DINOv2. We add LoRA to the query and value projection matrices of the self-attention block in the last layer. That is, the new query \mathbf{q} and value \mathbf{v} for a token \mathbf{x} are obtained as

$$\mathbf{q} = W^Q \mathbf{x} + \Delta W^Q \mathbf{x}, \mathbf{v} = W^V \mathbf{x} + \Delta W^V \mathbf{x}, \quad (4)$$

$$\Delta W^Q = B^Q A^Q \quad \Delta W^V = B^V A^V, \quad (5)$$

where $B^Q, B^V \in \mathbb{R}^{D \times R}$ and $A^Q, A^V \in \mathbb{R}^{R \times D}$. To make $\Delta W^Q, \Delta W^V$ the low-rank approximations of the original query and value projection matrices, we set R to 4, which is much smaller compared to the original feature dimension D (768 for DINOv2) of the model.

To train the models on *DepthCues* tasks, we attach a two-layer MLP with an intermediate GELU activation [32] and output neurons corresponding to the tasks. The models (LoRA weights and the MLP) are trained for around 15,000 iterations using AdamW [40] optimizer with cosine learning rate decay and a batch size of 32. The learning rate is set to 10^{-5} at the start and warms up to 10^{-3} .

D. Evaluated Models

Here we describe each model we evaluated in *DepthCues*, grouped by the supervision type. We summarized the architecture, supervision, and training dataset, along with the median rank (m-Rank) of each model in Tab. A4. The median rank is calculated based on the model’s rank for each cue. For all models, we used publicly available checkpoints provided by the official codebases or from the timm [73] or transformers [74] Python libraries.

Categorization. The following models are trained for image classification problems with category labels using the ImageNet dataset [14]. ResNet18 (RN18) and ResNet50 (RN50) [29] are convolutional neural networks with residual connections. ResNext50 (RNx50) [76] and SENet (SENet154) [35] are extensions of residual convolutional networks, offering improved efficiency and scalability. ConvNext (ConvNext-b) [49] is also designed with convolutional blocks, but its design choices are reconsidered based on the success of recent transformer-based [15] models. ViT (ViT-b16) [15] and DeiT III (DeiT-b16) [68] are transformer-based image models built on multi-head attention. We use the base configuration with 16 patch sizes for both models.

Depth. MiDaS (MiDaS-I16) [59] and DepthAnythingv2 (DepthAnyv2-b14) [78] are models trained with dense depth supervision. Both models use transformer architectures and are trained on a mix of datasets containing dense depth supervision for pixel values. The encoder network of DepthAnythingv2 is initialized with DINOv2 [55], while MiDaS is trained from scratch.

Segmentation. SAM (SAM-b16) [41] is trained on a large-scale segmentation dataset that provides dense pixel-level category information.

Language. CLIP (CLIP-b16) [57] and SigLIP (SigLIP-b16) [80] are trained to align the representations of images with their textual descriptions with a contrastive objective. StableDiffusion (SD2.1) [61] is a diffusion-based generative network that produces images conditioned on text descriptions. It is trained on a large-scale dataset [62] containing image-text pairs.

Multi-View. CroCo (CroCo-b16) [72] is trained with a cross-view completion objective using multi-view images, where the task involves predicting a patch of an image from another view. DUS3R (DUS3R-I16) [70] addresses the 3D reconstruction task for the generalized stereo case using neural networks through direct regression. It takes multi-view images as input and predicts dense 2D-3D point mappings for each view. LRM (LRM-b14) [33] is a large-scale 3D reconstruction network that takes images as input and outputs 3D representations. The network is trained with direct supervision using a large-scale 3D object repository [13].

Self-Supervised. MAE (MAE-b16) [30] and DINO (DINO-b16) [10] are trained with masked and contrastive self-supervised objective terms, respectively, without using any human-provided labels. iBOT (iBOT-b16) [84] and DINOv2 (DINOv2-b14) [55] combine masked and contrastive objectives to train networks. All of these methods are based on the transformer [15] architecture with the base configuration.

m-Rank	Model	Architecture	Supervision	Dataset (Size)
17.5	ResNet18 [29]	ResNet	Category	ImageNet (1.2M)
16	ResNet50 [29]	ResNet	Category	ImageNet (1.2M)
15	ResNext50 [76]	ResNet	Category	ImageNet (1.2M)
16.5	SENet [35]	ResNet	Category	ImageNet (1.2M)
11.5	ViT [15]	ViT-B/16	Category	ImageNet (14M)
6.5	DeiT III [68]	ViT-B/16	Category	ImageNet (14M)
12.5	ConvNext [49]	CNXT-B/16	Category	ImageNet (14M)
17.5	MAE [30]	ViT-B/16	Self-Supervised	ImageNet (1.2M)
5	iBOT [84]	ViT-B/16	Self-Supervised	ImageNet (14M)
9	DINO [10]	ViT-B/16	Self-Supervised	ImageNet (1.2M)
2	DINOv2 [55]	ViT-B/14	Self-Supervised	LVD (142M)
6.5	StableDiffusion [61]	UNet	Language	LAION (5B)
8	MiDaS [59]	ViT-L/16	Depth	MIX-6 (1.9M)
1	DepthAnythingv2 [78]	ViT-B/14	Depth	MIX-13 (0.5M+62M)
14.5	LRM [33]	ViT-B/14	Multi-View & 3D	Objaverse (10M), MVImgNet (6.5M)
14	CroCo [72]	ViT-B/16	Multi-View & Self-Supervised	Habitat (1.8M)
3.5	DUST3R [70]	ViT-L/16	Multi-View & 3D	MIX-8 (8.5M)
11.5	SAM [41]	ViT-B/16	Segmentation	SA (1B)
20	CLIP [57]	ViT-B/16	Language	LAION (2B)
7.5	SigLIP [80]	ViT-B/16	Language	WebLI (18B)

Table A4. **Evaluated vision models.** We consider a range of publicly available large vision models that span several forms of supervision. In most cases, we select checkpoints of comparable model and training size. We also report the median rank (m-Rank) of each model, which is calculated based on the model’s rank for each cue in *DepthCues*.